A thalamic reticular circuit

for head direction cell tuning

and spatial navigation

Authors: Gil Vantomme, Zita Rovó, Romain Cardis, Elidie Béard, Georgia Katsioudi, Angelo Guadagno, Virginie Perrenoud, Laura MJ Fernandez, Anita Lüthi*

*Lead contact

Affiliations: Department of Fundamental Neurosciences, University of Lausanne, Rue du Bugnon 9, 1005 Lausanne, Vaud, Switzerland

Summary

To navigate in space, an animal must reference external sensory landmarks to the spatial orientation of its body and head. Circuit and synaptic mechanisms that integrate external cues with internal head-direction (HD) signals to drive navigational behavior remain, however, poorly described. We identify an excitatory synaptic projection from the presubiculum and retrosplenial cortex to the anterodorsalmost sector of the thalamic reticular nucleus (TRN), so far classically implied in gating sensory information flow. Projections to TRN showed driver characteristics and involved AMPA/NMDA-type glutamate receptors that initiated TRN cell burst discharge and feedforward inhibition of anterior thalamic nuclei, where HD-tuned cells relevant for egocentric navigation reside. Chemogenetic anterodorsal TRN inhibition broadened the tuning of thalamic HD cells and compromised egocentric search strategies in the Morris water maze. Besides sensory gating, TRN-dependent thalamic inhibition is an integral part of limbic navigational circuits to recruit HD-cell-dependent search strategies during spatial navigation.

Keywords: Anterior thalamus; Retrosplenial cortex; Presubiculum; Allocentric; Egocentric; Synaptic inhibition; Burst discharge; Perseverance; Optogenetics; Chemogenetics

Correspondence: anita.luthi@unil.ch

Introduction

26

27 Spatial navigation requires the ability to notice environmental landmarks, detect their sensory

28 characteristics, and set these in relation to one's self-perceived direction, speed, and location.

29 Cortex is a major site for spatial sensory processing and for creating internal representations of

30 space based on one's own movement, location and body orientation to guide navigation.

31 However, in the interest of survival, environmental cues may need to be detected rapidly to adapt

32 navigational strategies without potentially time-consuming cortical elaboration. A major site for

33 subcortical gating of sensory stimuli is the inhibitory thalamic reticular nucleus (TRN) that shows

34 a unique anatomical positioning at the interface between sensory thalamic nuclei and cortex

35 (Scheibel and Scheibel, 1966; Pinault, 2004; Crabtree, 2018). The significance of TRN in

36 controlling sensory flow is now documented for the gain control of incoming sensory inputs (Le

37 Masson et al., 2002), the sharpening of receptive fields (Lee et al., 1994; Soto-Sánchez et al.,

38 2017), attentional modulation of monomodal (Halassa et al., 2014) or multimodal conflicting

39 sensory inputs (Ahrens et al., 2015; Wimmer et al., 2015), and sensory induced escape (Dong et

40 al., 2019).

41 In contrast to its role in sensory gating, the TRN has not been implied in the gating of internal

42 signals that underlie one's sense of orientation in space. Lesion studies, however, suggest that

43 TRN contributes to covertly directing a rat's self-orientation to the target stimulus, such that

44 orienting movements can be rapidly executed (Weese et al., 1999). Moreover, anterior thalamic

45 nuclei (ATN) are part of the brain's navigational system (Dumont and Taube, 2015), and there is

46 anatomical evidence in rodent that anterodorsal TRN innervates ATN (Scheibel and Scheibel,

47 1966; Gonzalo-Ruiz and Lieberman, 1995b, a; Lozsádi, 1995; Pinault and Deschênes, 1998),

48 although this has been questioned in cat (Paré et al., 1987). The anterodorsal (AD) thalamic

49 nucleus, part of the ATN, contains a large proportion of HD cells tuned to the direction of the

50 rodent's head in space (Taube, 1995), which serve as an egocentric, self-centered compass

51 during navigation (van der Meer et al., 2010; Butler et al., 2017). Although the TRN has been

52 proposed to be part of HD circuits (Peyrache et al., 2019), the underlying functional anatomy

53 remains elusive. Possible equivalences and differences to the canonical sensory TRN-

54 thalamocortical circuits thus remain speculative and possible roles for TRN in the gating of HD

55 and spatial navigation signals have not been clarified. Here, we hypothesized that if the TRN is

56 to mediate subcortical sensory gating effectively, it should serve as an entry point for information

57 flow to ATN to control the processing of HD signals.

58 The anterior thalamic HD representation is controlled by external visual landmarks through input

59 from the dorsal presubiculum (dPreS) (Goodridge and Taube, 1997) and the retrosplenial cortex

60 (RSC) (Clark et al., 2010). Both areas are reciprocally connected (van Groen and Wyss, 1990)

61 and receive afferents from ATN, primary and secondary visual cortex, integrating information

62 relevant for egocentric and allocentric, external cue-guided, navigation (Dumont and Taube, 2015;

63 Clark et al., 2018; Mitchell et al., 2018; Simonnet and Fricker, 2018). Behaviorally, lesion of dPreS

64 compromises rapid orienting behaviors based on landmarks (Yoder et al., 2019), whereas RSC

65 lesions lead to multiple deficits in spatial navigation and memory formation (Clark et al., 2018;

66 Mitchell et al., 2018). Although there is evidence for a topographically organized cortical feedback

67 from RSC to rat and monkey anterodorsal TRN (Cornwall et al., 1990; Lozsádi, 1994; Zikopoulos

68 and Barbas, 2007), the nature of this cortico-thalamic communication has never been

69 characterized. Indeed, current models of HD circuits involving ATN, dPreS and RSC (Dumont

70 and Taube, 2015; Peyrache et al., 2017; Simonnet and Fricker, 2018; Perry and Mitchell, 2019)

71 and of the brain's 'limbic' navigational system (Bubb et al., 2017) largely disregard a functionally

72 integrated TRN. In spite of this gap of knowledge, the notion of a limbic anterior TRN has been

73 proposed recently (Zikopoulos and Barbas, 2012; Halassa et al., 2014).

74 In this study, we combined tracing techniques, *in vitro* and *in vivo* electrophysiological recordings

75 together with a spatial navigation task to probe the synaptic integration and the function of TRN

76 in the communication between PreS, RSC and ATN.

77

Results

79 **RSC and PreS send topographically organized projections to ATN and TRN**

80 To determine afferent projection to the anterodorsal portion of the TRN, we injected small volumes

81 (50-100 nl) of red retrobeads into anterodorsal TRN of C57BL6/J mice (4-8-week-old) and

82 identified sites of red punctate fluorescent labeling 5 – 7 days later. Five out of 19 injections were

83 restricted to the anterior TRN in its dorsalmost portion, as verified by parvalbumin (PV)-

84 immunostaining of the TRN (Fig. 1A1). Punctate labeling clearly separated from the injection site

85 was found in the adjacent anterodorsal (AD), laterodorsal (LD) and in the centrolateral (CL) nuclei

86 (Fig. 1A2, Suppl. Fig. 1), consistent with prior tracing studies (Gonzalo-Ruiz and Lieberman,

87 1995b, a; Lozsádi, 1995; Pinault and Deschênes, 1998). Labeling was also found in deep layers

88 of prelimbic cortex that extended into infralimbic and cingulate, and, in two cases, into motor

89 cortical areas, consistent again with a previous study in rat (Lozsádi, 1994). Our attention was

90 drawn to a distinct stretch of puncta extending from parahippocampal regions into RSC (Fig. 1A2).

91 Labeling included in particular the deep layers of the PreS that is interposed between the

92 subiculum, the parasubiculum and the RSC (Ding, 2013; Simonnet and Fricker, 2018).

93   We next used the anterograde tracer, *Phaseolus vulgaris*-leucoagglutinin (PHAL-L), to confirm
94   projections from RSC and PreS to anterior TRN. Through a panel of injections (n = 20) that
95   targeted restricted portions of RSC, dPreS and ventral PreS (vPreS) (Fig. 1B1), we noted a
96   nucleus-specific labelling pattern in the LD, AD, and anteroventral (AV) thalamus, which is also
97   part of ATN (Fig. 1B2). Injections centered within the RSC labeled large portions of AD and LD,
98   while sparing AV, whereas PreS-centered injections covered more restricted portions of LD, AD
99   and AV. vPreS injections labeled the most lateral portion of LD and AV. All labeled fibers arborized
100   within the most anterodorsal portions of TRN (Fig. 1B3), with fibers surrounding TRN cell bodies,
101   pointing towards putative synaptic connections.

The PreS/RSC establishes functional excitatory synapses onto TRN

103   We used whole-cell patch-clamp recordings to address the presence of functional connections
104   between PreS/RSC, anterodorsal TRN and ATN in acute coronal slices from brains of mice
105   injected with AAV1-CaMKIIa-ChR2-EYFP into PreS/RSC 3 – 5 weeks earlier (Fig. 2A). Cells
106   patched within anterodorsal TRN showed rebound burst behavior, as recognizable by repetitive
107   high-frequency bursts of action potentials after brief hyperpolarization, similar to posterior sensory
108   TRN cells (Fig. 2B) (Fernandez et al., 2018). Electrical properties were also similar to those of
109   their posterior counterparts (Fig. 2A-C), although cells produced less repetitive bursts (Fernandez
110   et al., 2018; Vantomme et al., 2019). Cells in AD, AV and LD showed properties typical for dorsal
111   thalamocortical neurons, notably the presence of only a single rebound burst discharge
112   (Huguenard, 1996) (Suppl. Fig. 2).

113   Optogenetic stimulation of PreS/RSC fibers was applied while recording from voltage-clamped
114   neurons of the anterodorsal TRN and of AD, AV and LD (Fig. 2D,E). The location of cells within
115   the different thalamic nuclei was evident while guiding the patch pipette to the target region and
116   was confirmed in a subgroup of cells through perfusion with neurobiotin and *post-hoc* recovery
117   (n=33/106) (Fig. 2D1). Rapid synaptic inward currents were elicited in all responsive cells (Fig.
118   2D2). The connectivity, quantified based on the presence of such synaptic currents in the
119   complete set of recorded cells, was > 80 % for all areas (Fig. 2D3). Synaptic currents were time-
120   locked to the stimulus, with a fixed and short latency to response onset and sub-millisecond jitter
121   (Fig. 2D4,D5). Response latency was inversely proportional to light intensity (Suppl. Fig. 2), which
122   is consistent with an action potential-dependent mode of synaptic transmission (Gjoni et al.,
123   2018). There is thus a direct, monosynaptic connection from PreS/RSC to anterodorsal TRN and
124   to AD, AV and LD.

125

126
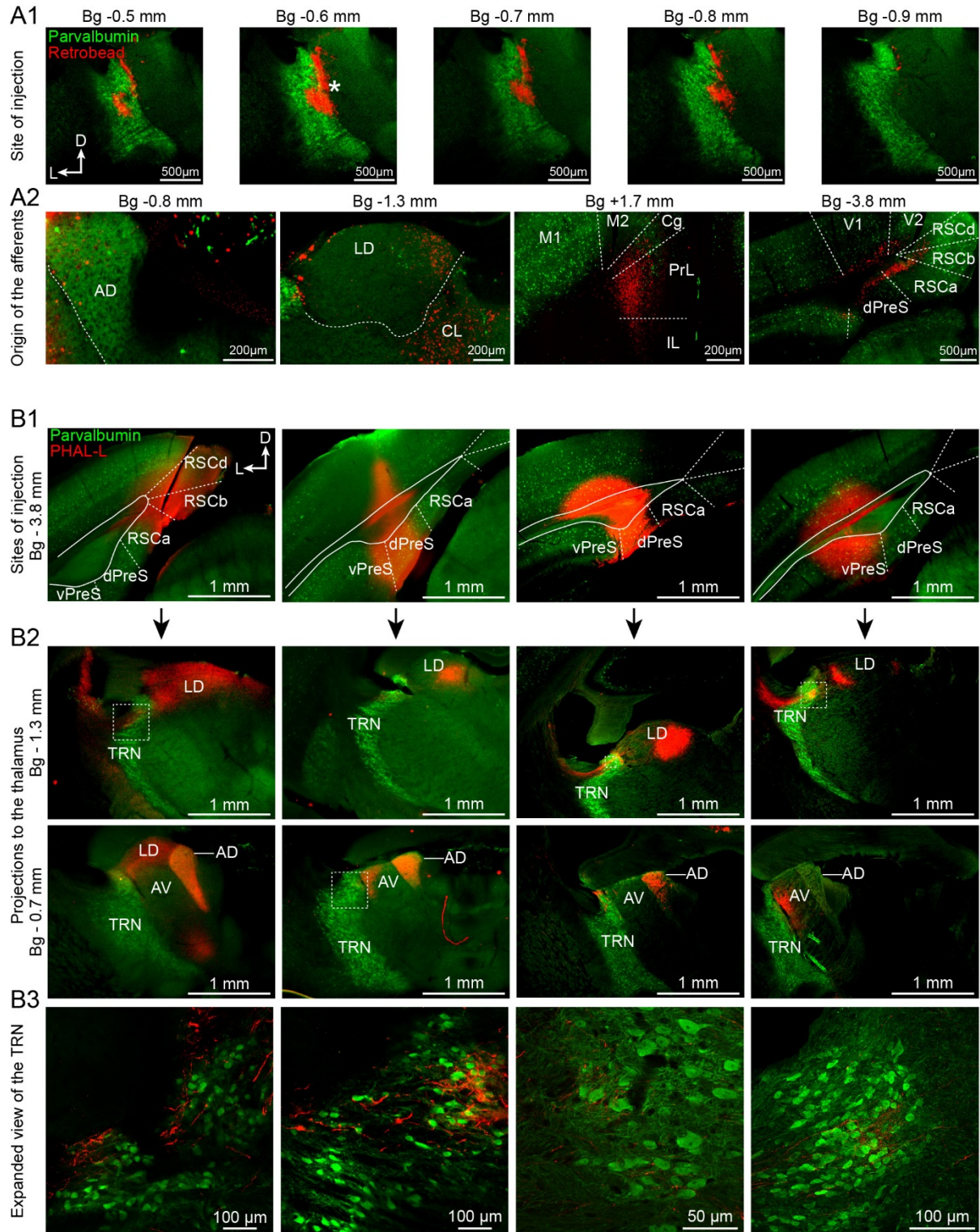
Figure 1. The RSC and the PreS send topographically organized projections to the anterior thalamus and TRN.

(A1) Epifluorescent micrographs of mouse coronal brain sections showing a retrobead (red) injection site (*) into the anterior portion of the TRN, which spread ~300 μm along the anteroposterior extent of the TRN (immunostained for PV, green). Bg, Bregma. **(A2)** Epifluorescent micrographs showing retrogradely labeled brain regions. Anterodorsal thalamus (AD) – Laterodorsal thalamus (LD) – Centrolateral thalamus (CL) – Cingulate cortex (Cg) – Prelimbic/Infralimbic cortex (PreL/IL) – dorsal Presubiculum (dPreS) – Retrosplenial cortex (RSC) – Visual cortex (V1/V2) – Motor cortex (M1/M2). **(B1)** Epifluorescent micrographs of 4 different injection sites of PHAL-L (red) into (from left to right) RSC, PreS, dPreS and ventral PreS (vPreS). Green, PV+ neurons. **(B2)** Epifluorescent micrographs of coronal sections in ATN at Bg -1.3 mm (top) and -0.7 mm (middle). Note labeled fibers visible in the anterodorsal TRN (dotted squares). **(B3)** Expanded confocal microscopy views of areas indicated by dotted squares in B2, AV, anteroventral thalamus.

Light-evoked postsynaptic currents (EPSCs) were mediated by glutamatergic synaptic receptors, as verified in a subset of 5 TRN and 5 neurons of AD, AV or LD (jointly referred to here as ATN+) (Fig. 2E1). Thus, the AMPA receptor antagonist 6,7-Dinitroquinoxaline-2,3(1H,4H)-dione (DNQX, 40 μM, bath-application) reduced responses by > 90 % at -60 mV (Fig. 2E1,E2). The block was not complete, suggesting activation of non-AMPA receptors. Indeed, a current component sensitive to the NMDA receptor antagonist DL-2-Amino-5-phosphonovaleric acid (APV) was detectable at +40 mV (Fig. 2E1, E2). NMDA/AMPA ratios were comparable to previous studies in sensory TRN and thalamus (Fernandez et al., 2017). Moreover, the TRN-EPSCs had a twice-shorter half-width than ATN+-EPSCs (Fig. 2E3) and a faster decay time (Fig. 2E4). PreS/RSC inputs thus convey a phasic excitatory input onto anterodorsal TRN cells.

PreS/RSC establishes strong unitary connections with driver characteristics onto anterodorsal TRN

TRN and ATN+ neurons were robustly innervated by PreS/RSC afferents, with compound EPSC amplitudes ranging from -25 pA to -1157 pA at high light intensities, although there were nucleus-specific differences (Fig. 3A). Both large and small EPSCs were obtained in slices from the same animals, excluding variable viral transduction as a major reason for this variability. To assess how variability was based on strength and connectivity of PreS/RSC afferents, we used minimal optogenetic stimulation through reducing light intensity to variably evoke failures and successful responses at comparable rates (mean failure rate 47±3 %) (Fig. 3B1). Unitary PreS/RSC EPSCs of TRN cells were 4- to 5-fold larger than the ones established onto AD and AV cells (Fig. 3B2). Dividing the maximally evoked EPSC amplitude by the unitary one, we calculated ranges of 1 –

163
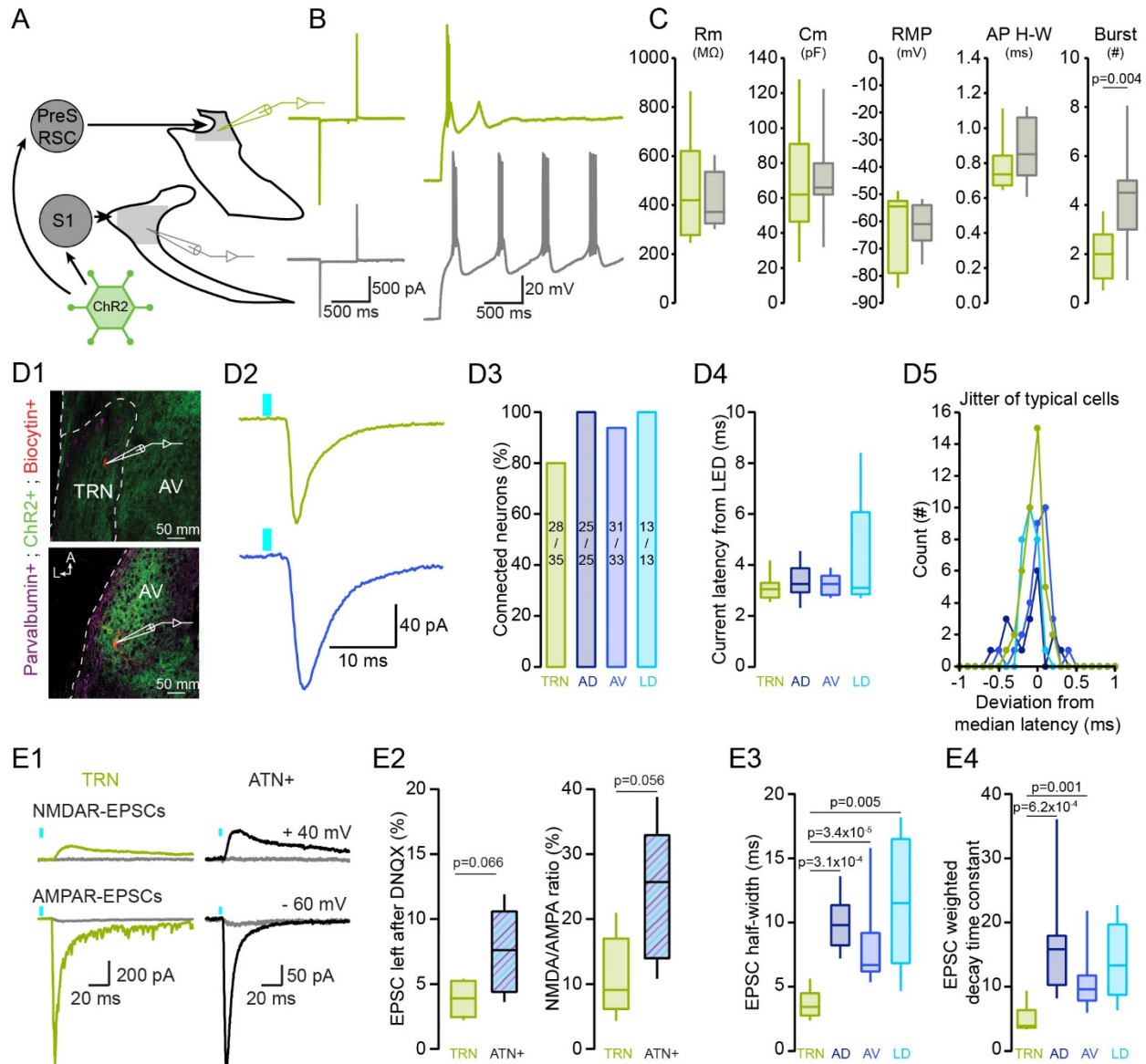
## Figure 2. The PreS/RSC establishes functional excitatory synapses onto TRN

(A) Scheme of viral injections (AAV1-CamKIIa-ChR2-EYFP) into PreS/RSC or primary somatosensory cortex (S1) followed by whole-cell patch-clamp recordings. **(B)** Responses of a PreS/RSC-connected TRN neuron (green) and a S1-connected TRN neuron (grey) to a 10 mV hyperpolarizing step in voltage-clamp (Left) and to negative current injection in current-clamp (Right). **(C)** Box-and-whisker plots of cellular properties of PreS/RSC-connected (n = 16) and S1-connected TRN neurons (n = 11). From left to right: Membrane resistance (Rm), membrane capacitance (Cm), resting membrane potential (RMP), action potential (AP) half-width (H-W), burst number. Mann-Whitney U tests were used for comparing Rm, RMP and AP H-W, Student's *t* tests for Cm and Burst number. Data from S1-connected TRN neurons re-used from a previous study (Fernandez et al., 2018) **(D1)** Confocal micrographs of 300 μm-thick mouse brain sections showing the whole-cell recorded TRN (top) and AV (bottom) neurons filled with neurobiotin (red). Green, ChR2-EYFP-expressing PreS/RSC afferents, magenta, PV+ TRN cells. **(D2)** Current

177 responses of TRN (top) and AV (bottom) neurons to optogenetic activation (blue bars, 1 ms, 3.5
178 mW power, 455 nm) of PreS/RSC afferents, recorded at -60 mV. **(D3)** Connectivity histogram,
179 calculated as the fraction (in %) of neurons responding to optogenetic stimulation. **(D4)** Box-and-
180 whisker plot of response latencies (calculated from LED onset, 'from LED') in the TRN (n = 12),
181 AD (n = 16), AV (n = 16) and LD (n = 6). Mann-Whitney U tests and Bonferroni correction: α =
182 0.0083. **(D5)** Jitter of response latencies (deviation from mean) in one cell from TRN, AD, AV and
183 LD across all stimulation trials. **(E1)** Pharmacological analysis of typical evoked excitatory
184 postsynaptic currents (EPSCs) in TRN and ATN+, showing AMPA- and NMDA-EPSCs and their
185 suppression by DNQX (40 μM) and APV (100 μM), respectively (superimposed grey traces). **(E2)**
186 Box-and-whisker plots of DNQX effects (left, in % of original response amplitude, n = 5 for both
187 TRN and ATN+) and of NMDA/AMPA ratios (right). Values of p from Student's *t* tests. **(E3)** Box-
188 and-whisker plot of EPSC half-widths for TRN (n = 7), AD (n = 8), AV (n = 14) and LD (n = 5).
189 Mann-Whitney U tests and Bonferroni correction: α = 0.0083. Statistically significant p values are
190 indicated. **(E4)** Box-and-whisker plot of the EPSC weighted decay time constant in TRN (n = 7),
191 AD (n = 8), AV (n = 14) and LD (n = 5). Same statistical analysis as E3.

192

193 19 fibers for TRN, 2 – 32 fibers for AD and 8 – 86 fibers for AV. Therefore, although variable, TRN
194 cells are, on average, targeted by a comparatively small number of fibers, but each with greater
195 unitary strength. A large unitary response size has also been described for cortical projections
196 onto sensory TRN (Golshani et al., 2001; Gentet and Ulrich, 2004; Cruikshank et al., 2010). To
197 determine how many of these fibers were necessary to bring TRN cells to threshold for action
198 potential firing, we performed cell-attached patch-clamp recording to preserve cellular integrity
199 during PreS/RSC synaptic stimulation (Fig. 3C1). Action current numbers showed a steep
200 sigmoidal light dependence with half-maximal values reached at 0.63 mW (Fig. 3C2,C3).
201 Subsequent whole-cell mode recording in 5 out of 6 cells confirmed that these were bursts of
202 action potentials riding on a low-threshold calcium spike, which showed similar light dependence
203 (half-maximal number of action potentials at 0.92 mW) (Fig. 3C1,C3). In particular, at a light
204 intensity corresponding to the one used for minimal stimulation (0.19±0.02 mW), single spikes
205 were riding on triangularly shaped calcium spikes. Single or few active synaptic inputs from
206 PreS/RSC appear thus sufficient to bring TRN cells to threshold through reliable EPSP-low
207 threshold burst coupling.

208 Excitatory afferents into thalamus have been divided into 2 major groups, drivers and modulators
209 (Sherman, 2017). To determine the nature of PreS/RSC afferents, we determined paired-pulse
210 ratios (PPRs) of TRN-and ATN+-EPSCs. Under our ionic conditions, PPRs remained close to 1
211 until at least 10 Hz (Fig. 3D1,D2, Suppl. Fig. 3). When plotting results from individual experiments,
212 all data points clustered around 1 for 1-10 Hz, supporting a homogeneity of fibers. This short-term
213 plasticity profile is characteristic for a driver input onto anterodorsal TRN, which is contrary to the

214
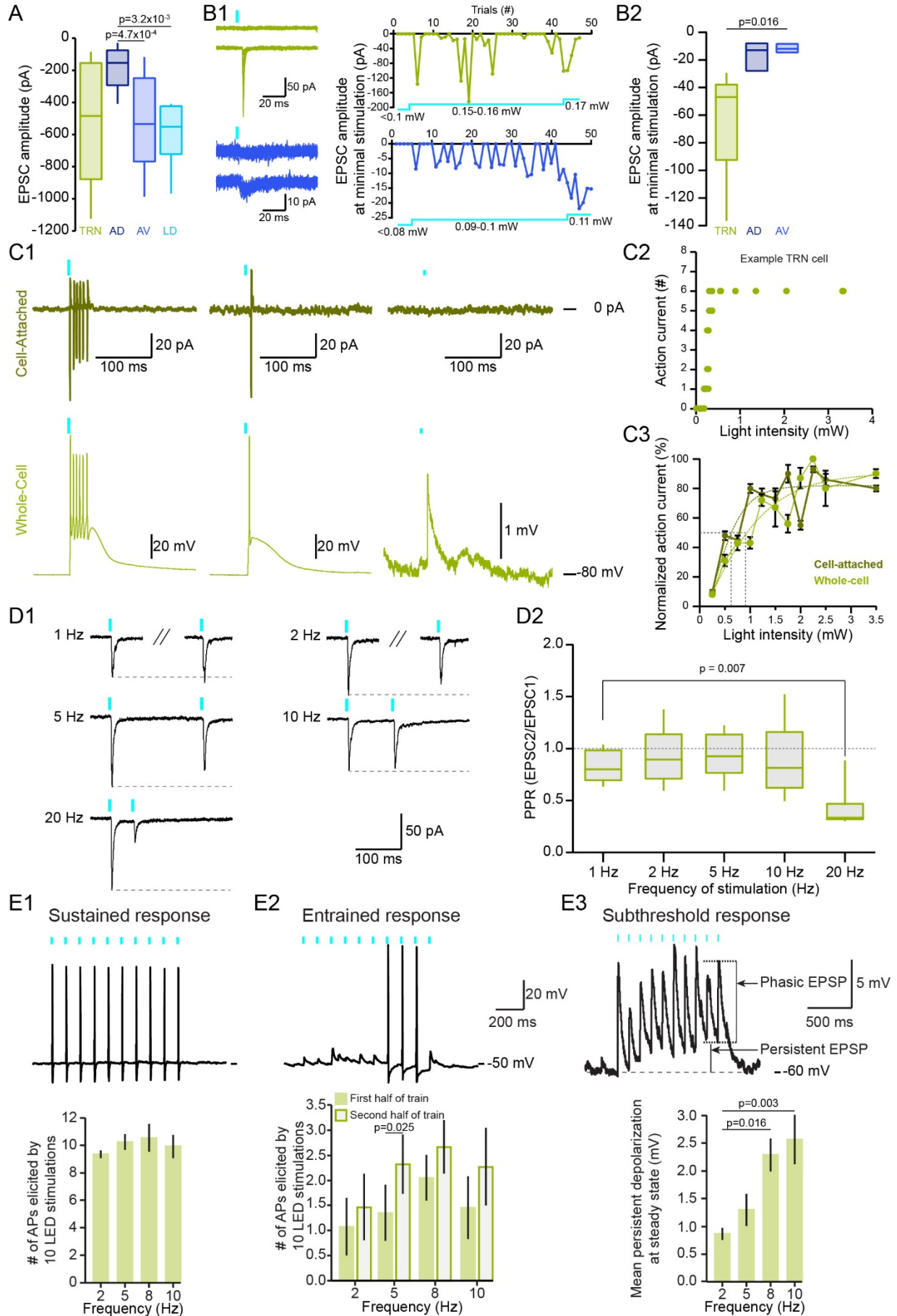
Figure 3. The TRN receives strong unitary connections with driver characteristics from the PreS/RSC.

(A) Box-and-whisker plot of maximally evoked compound EPSC amplitudes in TRN (n = 12), AD (n = 16), AV (n = 16), LD (n = 6). The intensity of the LED was reduced to ~20 % of the maximum in 4/16 AV and 4/6 LD cells to prevent escape currents. 1-factor ANOVA, p = 1.25x10^{-3}, post hoc Student's *t* tests with Bonferroni correction: α=0.0083. **(B1)** Minimal stimulation experiment. Left, overlay of successes and failures for a TRN and an AV neuron in one experiment. Right: Time course of the same experiment. Blue trace: intensity of the light stimulation. At minimal stimulation (0.15-0.16 mW for the TRN cell and 0.09-0.1 mW for the AV cell), the failure rate was ~50 % (22/39 failures for the TRN neuron, 20/39 failures for the AV neuron). Increasing the light intensity brought the failure rate to 0 % (right part of the graph). **(B2)** Box-and-whisker plot of the amplitude of successfully evoked unitary EPSCs in TRN (n = 5), AD (n = 3) and AV (n = 4). Repeated Mann-Whitney U tests with Bonferroni correction: α=0.017. **(C1)** Top: representative responses of a cell-attached TRN neuron recording exposed to maximal (left), intermediate (middle) and low (right) light intensities. Bottom: Same experiment in whole-cell current-clamp mode. **(C2)** Graph of action current number for the TRN neuron shown in C1. **(C3)** Same as in C2 for the average of all TRN neurons (cell-attached n = 6, whole-cell n = 5). Data were binned in 0.25 mW light steps. Action current number normalized to the maximum evoked in each neuron. **(D1)** RepresentativeTRN EPSCs at -60 mV upon paired-pulse stimulation at 1, 2, 5, 10 and 20 Hz. Grey dotted lines: amplitude of the first EPSC. **(D2)** Box-and-whisker plot of paired-pulse ratios (TRN: n = 16). Paired Student's t tests or Wilcoxon signed rank-test and Bonferroni correction: α = 0.013. **(E1)** Top: typical membrane voltage response of a TRN neuron to a 10 Hz-light stimulation train. Bottom: Histogram of means (n = 7). Wilcoxon signed rank-tests and Bonferroni correction: α = 0.017. **(E2)** Top: same as in E1 for neurons responding with a subthreshold response at train onset. Bottom: Histogram of means (n = 6). Wilcoxon signed rank-test (at 2 Hz) and Paired Student's *t* tests (at 5, 8, 10 Hz). **(E3)** Top: same as in E1 for subthreshold responses in a TRN neuron held at -60 mV. Bottom: Histogram of the mean persistent depolarization (n = 5). The persistent depolarization measured on the last 3 stimulations. 1-factor RM ANOVA, p = 0.033, post hoc paired Student's *t* tests and Bonferroni correction: α = 0.017.

modulatory profile of cortical input onto sensory TRN, showing paired-pulse facilitation (PPF) (Fernandez et al., 2018).

At depolarized potentials, where tonic discharge is prevalent, PreS/RSC afferents reliably sustained TRN discharge during stimulation trains (Fig. 3E1). Furthermore, initially subthreshold responses could become suprathreshold in the course of a train (Fig. 3E2), most likely due to temporal summation that gave rise to a persistent depolarization on top of the phasic events (Fig. 3E3). Similar results were found at PreS/RSC-ATN+ synapses (Suppl. Fig. 3).

PreS/RSC afferents mediate feedforward inhibition onto ATN+ through recruiting burst discharge in PV- and somatostatin (Sst)-expressing TRN cells

How does TRN recruitment by PreS/RSC afferents regulate ATN+ activity? We first tested *in vitro* for Pres/RSC-triggered feedforward inhibition onto ATN+ (Fig. 4A). ATN+ cells were held at

256 voltages to separately monitor EPSC and IPSC components (-60 mV and +15 mV) (see Methods

257 for further details). Out of 22 ATN+ neurons innervated by PreS/RSC, 19 (9 AD, 5 AV, 5 LD)

258 presented with a strong outward current at +15 mV, consistent with an evoked inhibitory

259 postsynaptic current (IPSC) (Fig. 4B). The IPSC latency was higher than the EPSC latency (Fig.

260 4C), consistent with a disynaptic feedforward inhibition. IPSCs were mediated through $GABA_A$

261 receptors (Fig. 4D1,D2). To demonstrate that these IPSCs were indeed mediated by anterodorsal

262 TRN, we combined opto- and chemogenetics in VGAT-Ires-Cre mice expressing the inhibitory

263 Designer Receptor Exclusively Activated by Designer Drugs (DREADD) specifically in the

264 GABAergic cells of anterodorsal TRN and ChR2 in PreS/RSC. Chemogenetic silencing of

265 anterodorsal TRN through bath-application of the DREADD ligand clozapine N-oxide (CNO) while

266 optogenetically activating PreS/RSC afferents indeed reduced the amplitude of the evoked IPSC

267 (Fig. 4E1,E2).

268 The TRN contains subnetworks of PV- or Sst-expressing cells with possibly different functions

269 (Clemente-Perez et al., 2017). We determined the contribution of these subnetworks to ATN+

270 inhibition using PV-Cre and Sst-Cre mice expressing ChR2 in anterodorsal TRN. ChR2-positive

271 fibers were visible throughout the AD, AV and LD in both mouse lines (Fig. 4F), and rapid IPSCs

272 were elicited by activation of both PV- and Sst-expressing TRN cells in all thalamic nuclei (Fig.

273 4G1,G2), suggesting a contribution of both subnetworks to ATN+ inhibition.

274 **Anterodorsal TRN activation regulates action potential firing in ATN+ and sharpens the**

275 **tuning of HD cells**

276 We next addressed the consequences of PreS/RSC activity on unit activity of ATN+ through *in*

277 *vivo* single unit recordings in freely behaving mice while optogenetically activating PreS/RSC

278 bilaterally (Fig. 5A-C). Firing patterns of single units in the ATN+ (n=28/42 responsive units from

279 3 mice), analyzed through raster plots, peri-event histograms and z-score analysis, fell into 4

280 distinct classes. The first group (n=5) diminished firing rate within a time window of 15 – 40 ms

281 that persisted for up to 65 ms (Fig. 5D1). The second group (n=7) showed a late increase in firing,

282 with an onset from the LED stimulation ranging from 25 – 140 ms and persisting for up to 45 ms

283 (Fig. 5D2), reminiscent of a rebound burst discharge. The third group, containing 1 unit only,

284 showed an increase in firing rate only within the first 15 ms after light offset (Fig. 5D3). The last

285 group (n=15) contained units with mixed responses that combined features of the first three

286 groups (Fig. 5D4). In 12 of the mixed cases (Fig. 5D5), inhibition preceded delayed excitation

287 (inhibition onset: 28±2 ms, rebound onset: 70±10 ms, Wilcoxon signed rank-test p = 3.90×10^{-5}).

288 Similarly, late increases in firing rate were clearly distinct in latency compared to the rapidly

289   responding units (early: 9±1 ms, late: 65±7 ms, Mann-Whitney U test p = 4.18x10^{-5}). Five out of

290   42 ATN+ units were tuned to the mouse's HD, as quantified by the length of the Rayleigh vector

291   (r) (r = 0.43±0.01, n=5) (Fig. 5E1) (see Methods, (Yoder and Taube, 2009)). PreS/RSC activation

292   induced a rebound firing in 2 of these (Fig. 5E2,E3). These results are consistent with a

293   feedforward inhibitory circuit recruited by PreS/RSC that is present throughout ATN+ and that
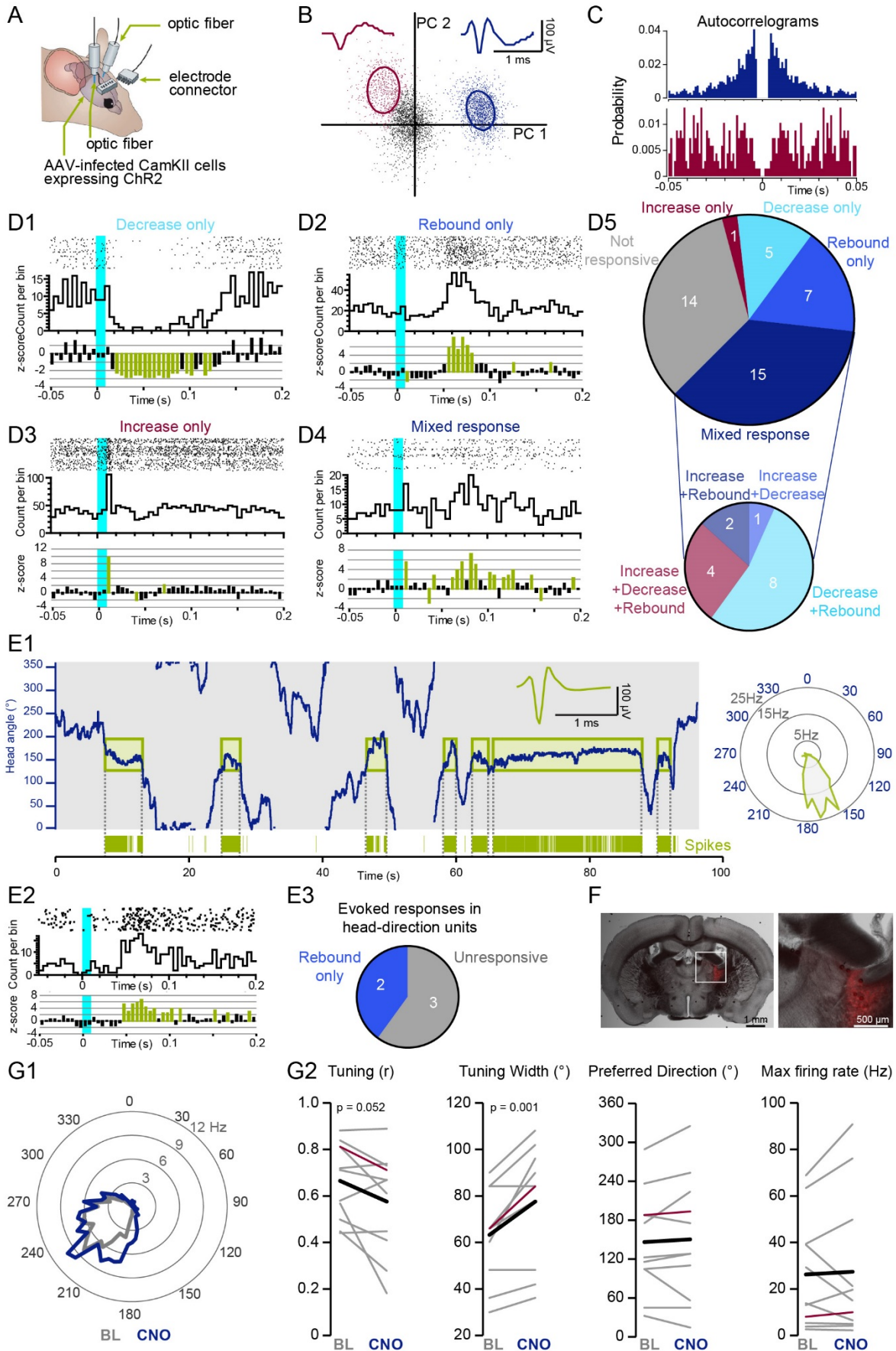
294   also targets HD cells.

295
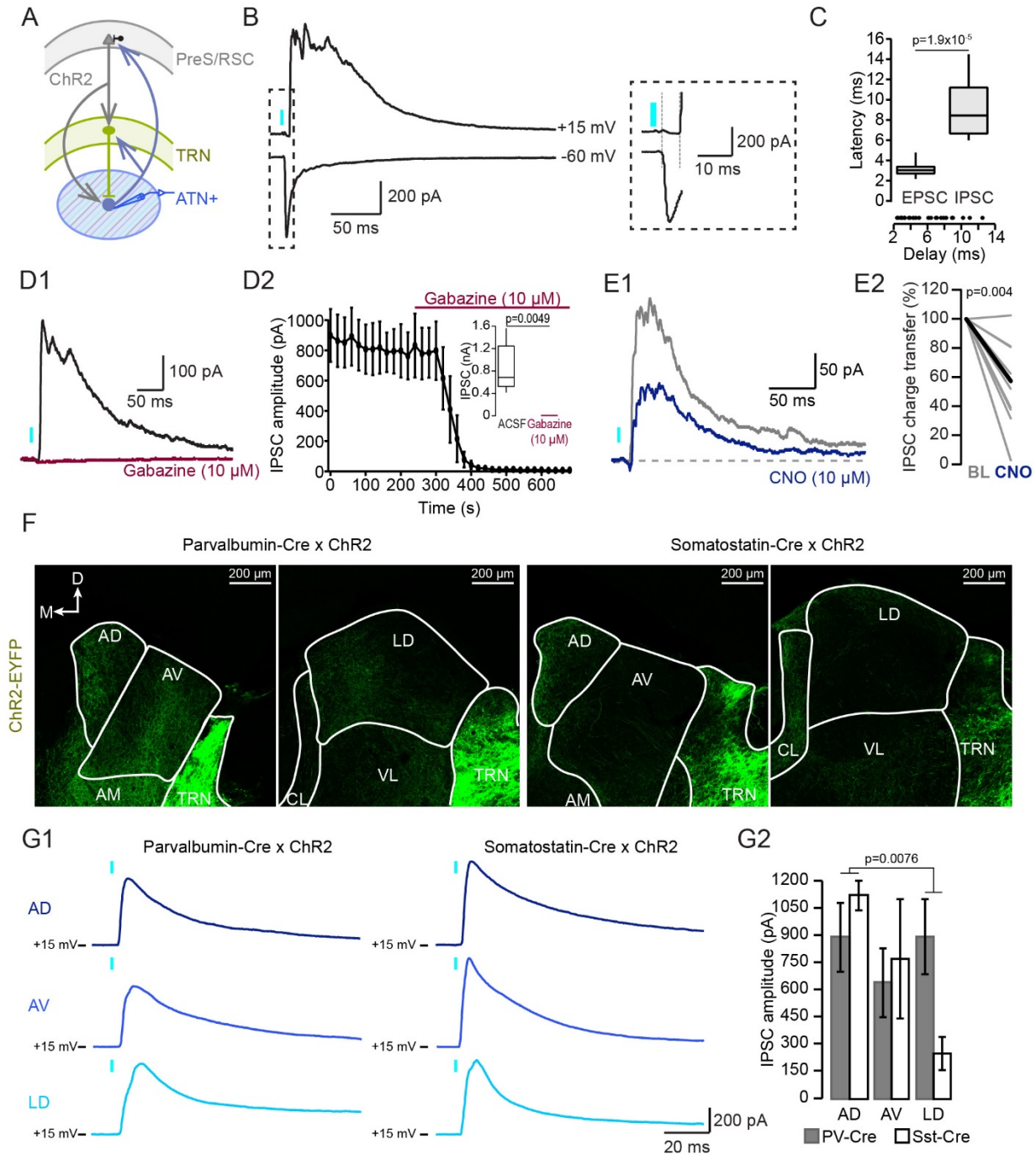
Figure 4. PreS/RSC afferents mediate feedforward inhibition onto anterior thalamus through recruiting burst discharge in PV- and Sst-expressing TRN cells.

(A) Scheme of the hypothesized circuit studied *in vitro*. **(B)** Typical current responses of an ATN+ neuron held successively at -60 and +15 mV to record EPSC and IPSC. Portion indicated by dotted rectangle is expanded on the right. Response latencies were measured from LED onset (grey vertical lines). **(C)** Top: Box-and-Whisker plot of EPSC and IPSC latencies in ATN+ neurons (n = 24). Bottom: Delays between the onset of the IPSC and the EPSC for all experiments. Wilcoxon signed rank-test. **(D1)** A typical ATN+ IPSC before (black) and after (red) bath-application of the GABA$_A$ receptor antagonist gabazine. **(D2)** Time course of gabazine action (n = 6). Inset: Box-and-Whisker plot of steady-state IPSC amplitude in ACSF and gabazine (paired Student's *t* test). **(E1)** IPSC evoked in an ATN+ neuron of a VGAT-Ires-Cre mouse expressing the inhibitory DREADD in anterodorsal TRN. IPSCs measured before (grey) and after (blue) 10 µM CNO bath-application. **(E2)** Representation of the charge transfer of IPSCs in ATN+ neurons (n = 10). Wilcoxon signed rank-test. **(F)** Confocal micrographs of ChR2-expressing PV-Cre (left) and Sst-Cre (right) coronal brain sections of ATN+. **(G1)** Representative IPSCs elicited in ATN+ neurons held at +15 mV. **(G2)** Histogram of IPSC amplitudes in AD (n = 6 for both PV- and Sst-Cre mice), AV (n = 6 for both) and LD (n = 6 for both). 2-factors ANOVA with factors 'nucleus' and 'cell type', p = 0.036 for 'nucleus', p > 0.05 for 'cell type', post hoc Student's *t* test with Bonferroni correction: α = 0.017 for IPSC amplitude between nuclei regardless of cell type.

Combining chemogenetic inhibition of anterodorsal TRN with silicone probe recordings targeted stereotaxically to the AD, the site of HD cells (Taube, 1995), we probed the role of anterodorsal TRN in further detail (Fig. 5F). Out of 22 sorted units, 11 were HD-tuned (Rayleigh r ≥ 0.4), 3 were head-modulated (0.2 ≤ r < 0.4) and 8 were untuned, similar to previously observed proportions (Taube, 1995; Yoder and Taube, 2009). We compared the tuning, tuning width, preferred direction and firing rate at the preferred direction of the HD units during a baseline session and 40 min after i.p. injection of CNO (1 – 2 mg/kg) (n=11) (Fig. 5G1,G2) or NaCl (n=10) (Suppl. Fig. 4). There was a trend for decreased tuning and a significant increase in the tuning width after CNO injection compare to baseline. NaCl injection did not induce changes in any of these parameters. There were no significant changes in preferred direction nor in firing rate with CNO nor NaCl. Therefore, the tuning curve of HD cells in AD in freely moving conditions deteriorates upon loss of TRN activity.

A optic fiber, electrode connector, optic fiber, AAV-infected CamKII cells expressing ChR2

B PC 2, PC 1, 100 μV, 1 ms

C Autocorrelograms

D1 Decrease only

D2 Rebound only

D3 Increase only

D4 Mixed response

D5 Increase only 1, Decrease only 5, Rebound only 7, Not responsive 14, Mixed response 15. Increase+Rebound 2, Increase+Decrease 1, Increase+Decrease+Rebound 4, Decrease+Rebound 8

E1 Head angle (°), Spikes, 25Hz 15Hz 5Hz, 100 μV 1 ms

E2

E3 Evoked responses in head-direction units. Rebound only 2, Unresponsive 3

F 1 mm, 500 μm

G1 12 Hz, BL, CNO

G2 Tuning (r) p = 0.052, Tuning Width (°) p = 0.001, Preferred Direction (°), Max firing rate (Hz), BL CNO

Figure 5. Anterodorsal TRN activation regulates action potential firing in anterior thalamus and sharpens the tuning of head direction cells.

(A) Scheme of the *in vivo* freely moving recording configuration. **(B, C)** Example of unit sorting based on principal component analysis (B) and autocorrelation (C). Autocorrelograms of the sorted units from panel B showing the typical refractory period around 0. **(D1-D4)** Raster plot, cumulative histogram and z-score analysis for four characteristic unit responses. **(D5)** Pie charts showing the proportion of the four characteristic responses in all putative thalamic units. **(E1)** Graph showing the mouse HD (blue trace) in combination with detected spikes of a putative thalamic HD unit (vertical green lines) tuned around 150°. Insets: mean unit waveform and a polar plot of the tuning curve. **(E2)** Example of a HD unit response to light activation of PreS/RSC afferents. **(E3)** Pie chart of the proportion of head-direction units responsive to light activation of PreS/RSC. **(F)** Sections for the anatomical verification of silicone probe implantation in VGAT-Ires-Cre mice expressing the chemogenetic silencer hM4D-mCherry (red) in anterior TRN. **(G1)** Polar plot of a HD unit's tuning curve during baseline (grey) and after injection of CNO (blue). **(G2)** Quantification of the changes in tuning parameters by CNO (n = 11 HD units). Far left: Rayleigh vector length size. Middle left: width of the tuning curve (measure at half the maximum firing rate). Middle right: preferred direction. Right: the firing rate at the preferred direction. Grey lines: single units. Red line: example unit from G1. Black line: average. Paired Student's *t* tests to compare data during baseline and 40 min after CNO injection.
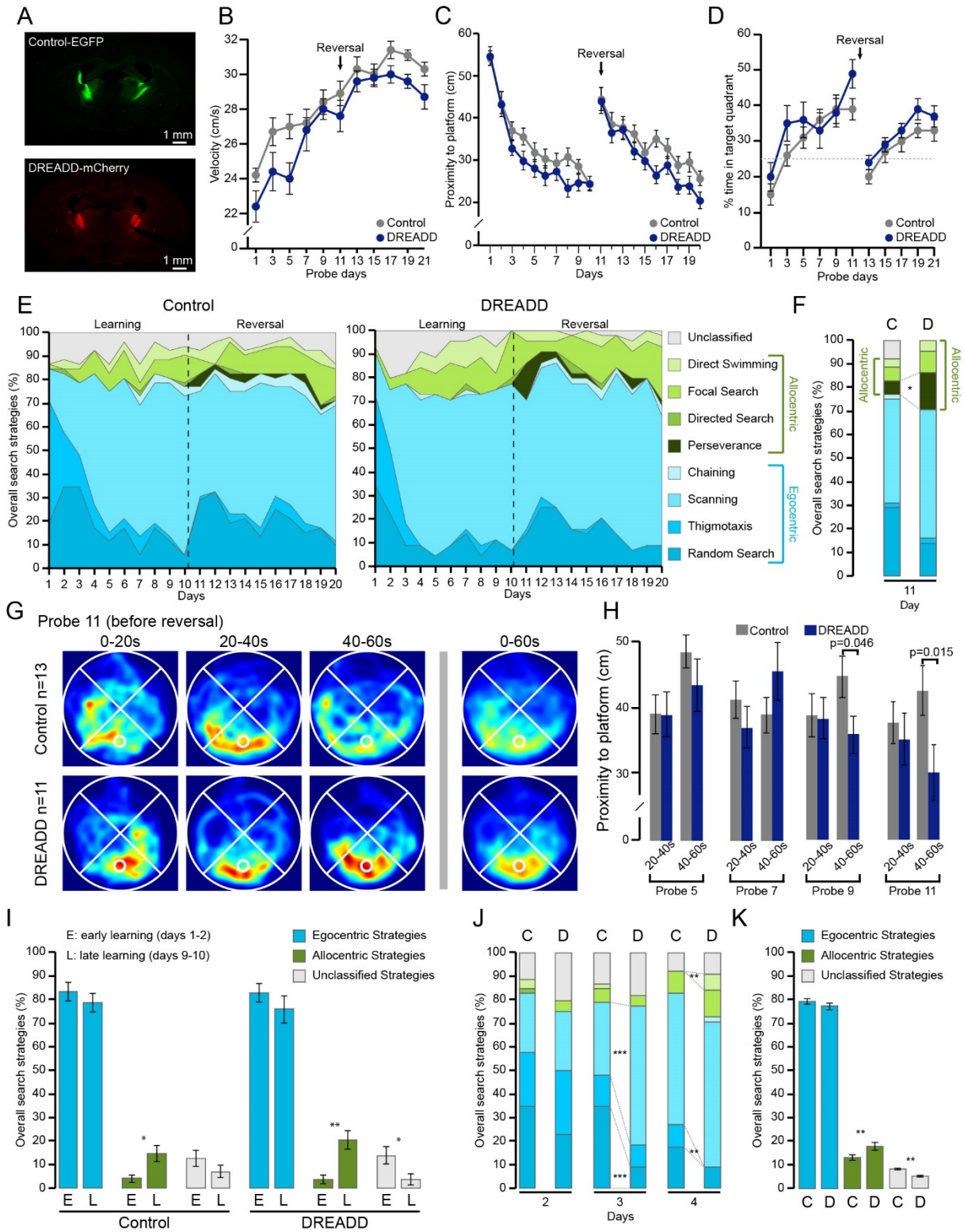
Anterodorsal TRN inhibition biases navigational search strategies in the Morris water maze

We chose the hidden platform version of the Morris water maze (MWM) to probe the role of anterodorsal TRN in spatial navigation. In this maze, both ATN-dependent egocentric and visual cue-dependent allocentric navigational strategies were reported (Stackman et al., 2012; Garthe and Kempermann, 2013). Mice were trained over 10 days to learn the hidden platform in a maze surrounded by visual landmarks, followed by a 10-day reversal learning during which the platform was located in the opposite quadrant (Suppl. Fig. 5A). We hypothesized that chemogenetic suppression of anterodorsal TRN activity, and reduction of PreS/RSC-mediated ATN+ inhibition, would alter navigational behavior once the animal had to rely on HD-dependent, egocentric strategies. We also asked whether there was a bias in search strategies already in the course of spatial learning.

We used two groups of mice: "control" VGAT-Ires-Cre and "DREADD" VGAT-Ires-Cre mice that expressed non-DREADD related proteins or the inhibitory DREADD specifically in the anterodorsal TRN, respectively (Fig. 6A). In each of the four daily test sessions, entry points into the maze were randomized across the quadrants to enforce the use of allocentric strategies. Both groups became faster swimmers in the course of the task and showed no significant difference in their mean swimming velocity during the 60-s probe sessions (with platform removed), although there was a light trend for control mice to be faster (Fig. 6B). We thus analyzed the proximity to

367 the platform instead of the latency to platform to account for possible effects of differences in swim
368 speed (Awasthi et al., 2019). Based on this measure, both groups performed similarly, as
369 indicated by a comparable decrease of the mean proximity to the platform during test sessions
370 (Fig. 6C). Moreover, from days 5 – 7 of training, the percentage of time spent in the target
371 quadrant was above chance level for both groups during probe sessions (Fig. 6D) These results
372 show an overall comparable, if not slightly better performance of DREADD mice, but they do not
373 provide information about the navigational strategies used. We hence classified swim trajectories
374 on a trial-by-trial basis for all test sessions according to previously described criteria for allo- and
375 egocentric strategies (Suppl. Fig. 6B-D) (Garthe and Kempermann, 2013; Rogers et al., 2017).
376 Figure 6E shows that mice use a mix of trajectories reflecting the use of both ego- and allocentric
377 strategies (Fig. 6E,I,K). Focusing first on early phases of reversal learning (day 11), DREADD
378 mice showed perseverance around the previous platform location, while control animals reverted
379 to trajectories consistent with egocentric strategies (Fig. 6F). If perseverance was indeed
380 reflecting a decreased ability to change navigational strategy once the correct platform location
381 was learned, signs of perseverance should also be seen in the course of learning. Indeed, when
382 inspecting time-binned occupancy plots during probe sessions, DREADD mice persevered
383 searching at the platform position for the whole 60 s-probe session, whereas control mice shifted
384 to a dispersed search pattern of other regions of the pool during the last 20 s of the session. This
385 was particularly the case during the last 2 probe sessions of the learning (beginning of day 9 and
386 11) (Fig. 6 G,H).

387 Inspired by the finding on the DREADD mice's possibly compromised ability to deploy egocentric
388 strategies during reversal learning, we asked whether evidence for biased strategy selection could
389 also be found during initial platform learning. As is characteristic for the MWM, there was an
390 increase in the proportion of allocentric strategies from day 1-2 to day 9-10 in both control and
391 DREADD mice (Fig. 6 I,J) (Garthe and Kempermann, 2013). However, DREADD mice did so in
392 temporal anticipation, showing significantly more scanning and less random search on day 3, and
393 more direct swimming and less thigmotaxis on day 4 (Fig. 6J). DREADD mice also used an overall
394 greater proportion of allocentric strategies across both learning and reversal learning than control
395 mice (Fig. 6K). Together, suppression of anterodorsal TRN activity 1) alters navigational behavior
396 at reversal learning and 2) biases the search patterns towards allocentric strategies during initial
397 learning.

398

399

Figure 6. Anterodorsal TRN inhibition biases navigational search strategies in the Morris water maze.

(A) Epifluorescent micrographs of VGAT-Ires-Cre mouse coronal brain sections at Bg -0.8 mm for a control mouse (top) and a test mouse (bottom). Color codes indicate expression products. **(B)** Mean swim velocities of control (n = 13) and DREADD (n = 11) mice during probe sessions. 2-factors RM ANOVA with factor 'day' and 'condition', p < 2x10^{-16} for 'day' and p = 0.04 for 'condition'. Post hoc Student's *t* tests with Bonferroni correction: α = 0.005 for 'condition': not significant. **(C)** Graph of the mean proximity to the platform during training sessions. 2-factors RM ANOVA with factor 'day' and 'condition', p < 2x10^{-16} for 'day' and p = 0.04 for 'condition'. Post hoc Student's *t* tests and Mann-Whitney U tests with Bonferroni correction: α = 0.003 for 'condition': not significant. **(D)** Graph of the percentage of time spent in the target quadrant during probe sessions. Chi-square test against 25% chance, significant at days 1, 7, 9, 11 for Control and days 5, 9, 11, 19, 21 for DREADD. **(E)** Stacked area graphs of search strategies used by control (left) and DREADD (right) mice during trial sessions. **(F)** Proportion of overall strategies at day 11 for control (C) and DREADD (D) mice. Chi-square tests for 'allocentric strategy' and for 'Perseverance', p < 0.05 for both. **(G)** Time-binned (20 s bins) and overall average occupancy plots during the last probe session of the learning phase. Hot colors indicate greater occupancy and are equally calibrated in all plots. **(H)** Histogram of the mean proximity to the platform of control and DREADD mice during binned-probe sessions. Student's *t* test for Control vs DREADD at late time bin (40 – 60 s). **(I)** Averaged proportion of egocentric, allocentric and unclassified strategies used during the early (E, days 1 and 2) and late (L, days 9 and 10) learning phase. Wilcoxon signed rank-tests, p = 0.02 for allocentric strategies in control mice, p = 0.008 and p = 0.03 for allocentric and unclassified strategies in DREADD mice, respectively. **(J)** Proportion of overall strategies at day 2, 3 and 4 for control (C) and DREADD (D) mice. Chi-squared tests for 'Scanning' and for 'Random Search' at day 3, p < 0.001 for both. Chi-square tests for 'Direct Swimming' and for 'Thigmotaxis' at day 4, p < 0.01 for both. **(K)** Averaged proportion of egocentric, allocentric and unclassified strategies used during the whole experiment. Student's *t* test comparing Control (C) vs DREADD (D).

Discussion

Anatomical and physiological identification of synaptic inputs to TRN has repeatedly opened a novel point of view for the TRN's active role in gating sensory information flow to and from the cortex (for review, see (Crabtree, 2018)). We uncover here a previously undescribed excitatory input to TRN from the parahippocampal dPreS and the RSC that shows high connectivity, mediates robust feedforward inhibition to ATN and shapes HD tuning in AD. These findings offer a possible synaptic mechanism contributing to the flexible use of navigational strategies during spatial learning and orientation. We thus identify here a novel thalamocortical loop that integrates TRN and that expands its gating function to the domain of self-orientation and navigation. More generally, we favor a view of the TRN as a multi-modal saliency selector that interfaces between acute cognitive demands, such as attentional switching or spatial re-orientation, and the recruitment of the appropriate sensory and self-orientational HD signals.

441 Retrograde tracing from the anterodorsal portion of the TRN identified several previously
442 described prefrontal cortical afferents (Cornwall et al., 1990; Lozsádi, 1994; Dong et al., 2019).
443 We now additionally demonstrate that there is a continuous band of afferent projections along the
444 presubicular-retrosplenial axis that starts at the border from subiculum to the PreS, thus at the
445 onset of the six-layered presubicular complex. These projections arise in deep layers of PreS and
446 RSC, to where projections to ATN were previously retrogradely traced (Wright et al., 2010). The
447 anterodorsal TRN seems thus to integrate visuospatial and HD input in combination with saliency
448 signals from prefrontal areas. The CL nucleus, a target of the superior colliculus, may convey
449 orienting-movement related signals into TRN (Krout et al., 2001). Moreover, central amygdalar
450 and hypothalamic inputs were recently described (Herrera et al., 2016; Dong et al., 2019).
451 Together, this adds to a complex web of afferents that contrasts with the predominantly
452 monomodal connectional characteristics of posterior sensory sectors of mouse TRN.

453 More work is required to elucidate the detailed organization of the anterodorsal synaptic
454 connectivity from PreS/RSC to anterodorsal TRN and from there to ATN. We note here that both
455 RSC and dPreS target LD and AD preferentially, while projections to AV are minor. AD and LD
456 are thought to functionally cooperate within the HD system (Simonnet and Fricker, 2018; Perry
457 and Mitchell, 2019), possibly acting as first- and higher-order nucleus, respectively (Peyrache et
458 al., 2019). The AV, together with the anteromedial nucleus, has been so far associated with a
459 theta-generating system innervated by vPreS (Perry and Mitchell, 2019). The limited spatial
460 resolution of our tracing methods does not currently allow to verify whether anterodorsal TRN is
461 also subdivided into sectors corresponding to this functional subdivision of ATN+. Interestingly,
462 single-cell labeling identified rat anterodorsal TRN cells with axons bifurcating to innervate both
463 AD and LD (Pinault and Deschênes, 1998). AM-projecting TRN cells were located more ventrally.
464 Anterodorsal TRN may thus contain cells jointly innervating AD and LD, further substantiating a
465 shared function.

466 Our characterization of a cortical excitatory innervation of TRN by PreS/RSC-excitatory input
467 reveals a combination of commonalities but also notable differences to the canonical form of
468 cortical input to sensory TRN that arises from layer 6 corticothalamic neurons of corresponding
469 primary cortex (Usrey and Sherman, 2019). Layer 6 synapses on TRN cells show a high
470 glutamate receptor content (Golshani et al., 2001), high unitary amplitude (Golshani et al., 2001),
471 faster rise and decay times (Gentet and Ulrich, 2004), smaller NMDA/AMPA ratios (Astori and
472 Lüthi, 2013) and marked PPF (Castro-Alamancos and Calcagnotto, 1999; Astori and Lüthi, 2013;
473 Crandall et al., 2015) compared to their thalamocortical counterparts. The presence of PPF

474 classifies layer 6 corticothalamic afferents as modulators rather than drivers (Sherman and

475 Guillery, 1998). While dPreS/RSC-TRN synapses are comparable in terms of unitary amplitude,

476 NMDA/AMPA ratio and EPSC waveform, there is a prominent lack of PPF at dPreS/RSC afferents

477 and a moderate entrainment of firing during repeated stimulation. Rather than being modulators,

478 the PreS/RSC inputs thus shares a short-term plasticity profile reminiscent of the driver inputs

479 that count as the principal information-bearing synapses. Top-down driver input is so far known

480 for corticothalamic layer 5 projections to higher-order thalamic nuclei that show a number of

481 morphological hallmarks (Usrey and Sherman, 2019). A driver profile that we suggest here for the

482 first time for TRN implies that anterodorsal TRN conveys direct system-relevant information that

483 is faithfully transmitted to its projection targets. We cannot exclude, however, that PreS and RSC

484 afferents, if stimulated separately, would show different short-term plasticity including PPF. A

485 further noteworthy point is that both PV+ and Sst+ TRN neurons innervate the AD, AV and LD

486 with comparable strength, pointing to functional differences compared to sensory first-order

487 thalamic nuclei (Clemente-Perez et al., 2017).

488 About 65% of ATN+ units showed a suppression of activity upon PreS/RSC stimulation that was

489 occasionally followed by a rapid increase in discharge. The timing of the inhibition-rebound events

490 is typical for a feedforward inhibitory mechanism (Crandall et al., 2015). Moreover, chemogenetic

491 TRN inhibition degrades HD cell tuning. The rather small effect size may be explained by the only

492 partial reduction of feedforward inhibition by CNO (see Fig. 4E). The anterodorsal TRN is thus

493 part of the top-down circuit so far thought to innervate the ATN+ only monosynaptically (Dumont

494 and Taube, 2015; Peyrache et al., 2017; Simonnet and Fricker, 2018; Perry and Mitchell, 2019).

495 This result advances the mechanistic understanding of the proposed update of thalamic HD cell

496 tuning by visual landmarks (Dumont and Taube, 2015). TRN-dependent inhibition may regulate

497 single AD cells, for example through promoting bursting, which we also observe *in vitro*, although

498 their existence *in vivo* has been questioned (Sheroziya and Timofeev, 2014). Bursting would

499 increase their impact in upstream navigational circuits, in particular in the dPreS circuits

500 (Peyrache et al., 2015), similar to what has been described for sensory thalamocortical circuits

501 (Sherman, 2001). TRN-mediated burst promotion in some AD neurons coupled with inhibition of

502 others could underlie the proposed increase in the precision of HD coding (Peyrache et al., 2015).

503 TRN-driven ATN bursting might also be an important component in oscillatory patterns observed

504 within ATN+, such as the one proposed to occur in AD (Peyrache et al., 2015; Peyrache et al.,

505 2019) or in AV (Tsanov et al., 2011), which are probably relevant for linking spatial information to

506 hippocampal memory processing.

507   To date, behavioral evidence for a role of the HD system in behavioral navigation is limited (Taube
508   et al., 1992; van der Meer et al., 2010; Valerio and Taube, 2012; Butler et al., 2017) and the role
509   of specific HD circuits, including dPreS and RSC, just starts to be behaviorally explored.
510   Experimental effort typically targets egocentric strategies, for example by moving the MWM
511   relative to landmarks between trials (Stackman et al., 2012), by studying navigation in darkness
512   (Yoder et al., 2019) or by putting rats upside down (Calton and Taube, 2005). In contrast, the idea
513   that spatial navigation requires an on-going switching between a range of possible strategies has
514   not been much pursued, although it is known for human studies (Miniaci and De Leonibus, 2018).
515   For example, a recent study using a hippocampus-specific synaptic knockout animal interpreted
516   perseverant behavior at the platform location as a lack of forgetting (Awasthi et al., 2019), but the
517   question of possible bias in navigational strategies was not addressed. Trajectory analysis in the
518   MWM thus offers itself as an interesting approach to follow on the evolution of navigational
519   behavior under well-controlled landmark conditions while simultaneously allowing egocentric
520   strategies (Dolleman-van der Weel et al., 2009; Garthe and Kempermann, 2013). We found a
521   preferential use of allocentric strategies when anterodorsal TRN was suppressed, suggesting that
522   egocentric navigation was less efficient. This is reminiscent of an ATN lesion study (Stackman et
523   al., 2012), although we cannot currently exclude that TRN-dependent inhibitory effects on nuclei
524   other than ATN, such as on intralaminar nuclei (Dong et al., 2019), contribute. Anterodorsal TRN
525   activity is required for qualitatively high HD signals in AD and/or for a robust activation of these
526   by feedforward inhibition. Anterodorsal TRN activity seems to be critically required at moments
527   when there is a mismatch between allocentric cues and new platform location, such that novel
528   relations between external landmarks and self-perceived orientational strategies, which depend
529   on HD cells, have to be built. Interestingly, the RSC has been proposed as an area involved in
530   allocentric navigation and memory formation, but also in the switching between allo- and
531   egocentric strategies to optimize navigational goals (Mitchell et al., 2018). In particular, its strong
532   connections to limbic thalamus have been implied in the solving of spatial problems (Clark et al.,
533   2018). Similar more complex roles in spatial navigation have recently been proposed for dPreS
534   (Yoder et al., 2019), which has been primarily analyzed as part of the hierarchy of the egocentric
535   coding system (Taube et al., 1990; Dumont and Taube, 2015; Peyrache et al., 2017). Our work
536   does not currently disentangle between the distinct roles of these two brain areas. However, it
537   has managed to pinpoint to the existence of a possibly fine switching mechanism at the interface
538   between major allocentric and egocentric brain areas that, when perturbed, preserved overt
539   navigational performance but compromised it at challenging moments that could pose existential
540   threats.

541   This work integrates TRN function into the brain's balanced control of sensory-guided spatial
542   navigation. The anterodorsal sector of TRN, located at the *limbus*, the 'edge' of the TRN, is a site
543   of complex integration where navigational, attentional, motor and emotional information may be
544   combined for precise activation of egocentric navigation systems. As a perspective arising from
545   this work, we suggest that neuropsychological screening for egocentric navigation deficits may
546   be useful in the diagnosis of disorders linked to TRN dysfunction, such as in neurodevelopmental
547   disorders linked to attentional deficits (Krol et al., 2018) and in schizophrenia (Wilkins et al., 2017).

Acknowledgements

Author contributions

561   GV carried out and analyzed all experimental tracing, *in vitro*, *in vivo* and behavioral data, and
562   also contributed to the design of the *in vivo* and behavioral experiments. ZR gained first evidence
563   for the anatomical connectivity between dPreS/RSC and anterodorsal TRN and initiated the *in*
564   *vivo* unit recordings. RC wrote the Matlab code for the analysis of head-direction data and MWM
565   Strategy. EB contributed to viral injections and the MWM experiments, GK to the antero- and
566   retrograde tracing data. AG carried out the *in vitro* recordings in PV- and Sst-Cre mice. VP
567   assisted with anatomical analysis. LMJF contributed to the surgery and analysis for *in vivo*
568   experiments. AL supervised the project and wrote the manuscript with contribution of GV.

Declaration of interests

570   The authors declare no competing interests.

STAR Methods

Animal husbandry and ethical approval

We used mice of either sex from the C57BL6/J line and from the Slc32a1$^{tm2(cre)Lowl}$ line, commonly referred to as VGAT-Ires-Cre line (Jackson Labs, generated by Dr. B. Lowell, Beth Israel Deaconess Medical Center, Harvard) (Vong et al., 2011), male C57Bl/6J;129P2_Pvalbtm1(cre)Arbr/J mice, referred to here as PV-Cre mice, and male B6N.Cg-Sst<tm2.1(cre)Zjh>/J mice, referred to here as Sst-Cre mice. These three transgenic lines express the Cre-recombinase either in VGAT-, PV- or Sst-positive neurons, respectively. All animals were housed in a temperature and humidity-controlled animal house with a 12/12 h light-dark cycle (lights on at 9 a.m.) and water and food available *ad libitum.* The VGAT-Ires-Cre line was originally generated on a mixed C57BL/6;FVB;129S6 genetic background and backcrossed to C57BL6 ever since. PV-Cre and Sst-Cre lines were maintained on a C57BL6 background. VGAT-Ires-Cre and PV-Cre were used as homozygous, whereas the Sst-Cre mice were heterozygous. For anatomical tracing (retrograde and anterograde), mice (n = 24) were transferred into a housing room with similar conditions on the day prior to injection. They remained there for 7 days after injection before perfusion and tissue processing. For viral injections, mice were transferred into a P2 safety level housing with similar conditions on the day prior to the injection. They remained there 3 – 5 weeks before being used for *in vitro* electrophysiology (n = 57), 2 – 3 weeks before surgical implantation for *in vivo* electrophysiology (n = 5), and 2 – 3 weeks before behavioral experiments (n = 24, only males). All experimental procedures complied with the Swiss National Institutional Guidelines on Animal Experimentation and were approved by the Swiss Cantonal Veterinary Office Committee for Animal Experimentation.

Anatomical tracing and verification of recording and injection sites

Retrograde tracing

C57BL6/J mice, 4- 8-week-old, were anesthetized with 5 % isoflurane and fixed onto the stereotaxic frame. During the surgery, the anesthesia level was reduced to 1- 3 % and N_2O was added if the surgery lasted > 1 h. Analgesia was ensured through Carprofen (5 mg/kg i.p.). Craniotomies were performed above the sites of injection at (anteroposterior (AP), mediolateral (ML), depth from cortical surface (DV), in stereotaxic coordinates from Bregma): -0.7, ±1.5, -3.1 to target the anterodorsal TRN. Glass pipettes (5-000-1001-X, Drummond Scientific, Broomall,

602 PA) were pulled on a vertical puller (Narishige PP-830, Tokyo, Japan) and backfilled by capillarity

603 with fluorescent latex microspheres (Red Retrobead™, Lumafluor). Using a Picospritzer III,

604 pressurized air pulses (15 psi, 10 ms) were applied every 10 s for 10 min to inject the retrobeads.

605 After 4 – 7 days, mice were perfused and their brains collected for immunostainings.

Anterograde tracing

607 The anesthetic and surgical procedures were the same as the ones used for retrograde tracing.

608 The coordinates of injection were (AP, ML, DV): -3.8, ±1.6, -1.0 for RSC, -3.8, ±2.3, -1.6 for PreS.

609 Glass pipettes were backfilled by capillarity with the plant lectin anterograde tracer *Phaseolus*

610 *vulgaris*-leucoagglutinin (PHAL-L, Vector Laboratories, Cat. No. L-1110). PHAL-L was chosen as

611 it permits focal labeling with little spread, which seemed appropriate to target PreS and RSC as

612 specifically as possible. A chlorinated silver wire was inserted into the pipette and a reference

613 electrode attached to the mouse tail. The PHAL-L was electroporated with a 5-µA current, 7 s

614 on/off loop for 20 min, applied with a home-made current isolator and a Master-8 (Master-8 Pulse

615 Stimulator, A.M.P.I., Jerusalem, Israel). After 5 – 7 days, mice were perfused and their brains

616 collected for immunostainings.

Perfusion and tissue processing

618 Mice were injected i.p. with a lethal dose of pentobarbital. Intracardial injection of ~45 ml of

619 paraformaldehyde (PFA) 4 % was done at a rate of ~2.5 ml/min. Brains were post-fixed in PFA 4

620 % for at least 24 h at 4°C. Brains were sliced with a Vibratome® (Microtome Leica VT1000 S,

621 section thickness: 100 µm, speed: 0.25-0.5 mm/s and knife sectioning frequency: 65 Hz) in 0.1 M

622 phosphate buffer (PB). Brain sections were either directly mounted on slides or disposed in

623 twelve-well plates filled with 0.1 M PB for immunohistochemistry.

Immunofluorescent labeling

625 100 µm-thick brain sections were washed 3 times in 0.1 M PB and transferred to a blocking

626 solution containing 0.1 M PB, 0.3 % Triton, 2 % normal goat serum (NGS) for 30 min. The first

627 antibody solutions also contained 0.1 M PB, 0.3 % Triton, 2 % NGS. For PHAL-L injected mice,

628 we added 1:8000x of rabbit anti-PHAL-L (Vector Laboratories, AS-2300, RRID: AB_2313686) and

629 1:4000x of mouse anti-PV (Swant, PV235, RRID: AB_10000343). For retrobead-injected and

630 virally injected PV-Cre and Sst-Cre mice, we added 1:4000x of mouse anti-PV (Swant, PV235,

631 RRID: AB_10000343). Sections were kept at 4°C for 48 h on a shaking platform. After 3 washings

632 in 0.1 M PB, we added a secondary antibody solution containing 0.1 M PB, 0.3 % Triton, 2 %

633 NGS and, when appropriate, 1:500x of goat anti-rabbit Cyanine Cy3™ (Jackson Immunoresearch,
634 111-165-003, RRID: AB_2338000), 1:500x of goat anti-mouse Cy5™ Jackson Immunoresearch,
635 115-175-146, RRID: AB_2338713) and/or 1:500x of goat anti-mouse Alexa Fluor® 488 (Jackson
636 Immunoresearch, 115-545-003, RRID: AB_2338840). Sections were mounted on slides and
637 covered with a mounting medium (Vectashield).

638 300 μm-thick brain sections obtained from patch-clamp recording sessions were post-fixed in 4
639 % PFA for at least 24 h. Brain sections were washed 3x in 0.1 M PB and then pretreated with a
640 solution containing 0.1 M PB and 1 % Triton for 30 min. The blocking solution was 0.1 M PB, 1 %
641 Triton, 2 % NGS and was applied for 30 min. The first antibody solution contained 0.1 M PB, 1 %
642 Triton, 2 % NGS, 1:4000x mouse anti-PV (Swant, PV235, RRID: AB_10000343) and was applied
643 for 5 days at 4°C. The secondary antibody solution contained 0.1 M PB, 0.3 % Triton, 2 % NGS,
644 1:500x goat anti-mouse CY5, (Jackson ImmunoResearch, 115-175-146, RRID: AB_2338713),
645 1:8000x Streptavidin ALEXA594 (Jackson ImmunoResearch, 016-580-084, RRID: AB_2337250)
646 and was applied for 24 h at 4°C. Sections were mounted on slides and covered with a mounting
647 medium (Vectashield).

648 ## Microscopy

649 Electromicrographs of brain slices were taken with a fluorescent stereomicroscope (Nikon SMZ
650 25) or a confocal microscope (Zeiss LSM 780 Quasar Confocal Microscope). NIS-Elements 4.5
651 (Nikon), Adobe Photoshop CS5 and Zen lite 2012 were used to merge images from different
652 channels.

653

654 **Viral injections**

655 Mice 3- 5-week-old were anesthetized using Ketamine-Xylazine (83 and 3.5 mg/kg, respectively)
656 and placed on a heating blanket to maintain the body temperature at 37°C. An initial dose of
657 analgesic was administrated i.p. at the beginning of the surgery (Carprofen 5 mg/kg). The animal
658 was head-fixed on a stereotactic apparatus equipped with an ear and mouth adaptor for young
659 animals (Stoelting 51925, Wood Dale, IL). The bone was exposed at the desired injection site
660 through a small skin incision. Viruses were injected with a thin glass pipette (5-000-1001-X,
661 Drummond Scientific, Broomall, PA) pulled on a vertical puller (Narishige PP-830, Tokyo, Japan).
662 C57BL6/J mice were injected bilaterally with a virus encoding ChR2 (500 nl of AAV1-hSyn-
663 ChR2(H134R)_eYFP-WPRE-hGH, 10^{12} GC, ~100–200 nl/min) into the PreS (AP, ML, DV): -3.8,
664 +/-2.5, -1.7. VGAT-Ires-Cre mice were injected bilaterally with 500 nl of AAV1-hSyn-

665 ChR2(H134R)_eYFP-WPRE-hGH (1×10^{12} GC, ~100–200 nl/min) into the PreS and/or unilaterally

666 or bilaterally with a virus encoding DREADD-mCherry (500 nl of AAV8-hSyn-DIO-

667 hM4D(Gi)_mCherry, 6.4×10^{12} GC), or DREADD-IRES-mCitrine (500 nl of ssAAV8/2-hSyn1-dlox-

668 A_hM4D(Gi)_IRES_mCitrine-dlox-WPRE-hGHp(A), 3.1×10^{12} GC) or a control AAV8 encoding a

669 DREADD-unrelated construct (500 nl of AAV8-hSyn-FLEX-Jaws_KGC_GFP_ER2, 3.2×10^{12} GC)

670 in the anterior sector of the TRN (AP, ML, DV: -0.8, ±1.35, -3.1). PV-Cre and Sst-Cre mice were

671 injected into the anterior TRN (AP, ML, DV: -0.8, ±1.35, -3.1) with AAV1-EF1a-DIO-

672 ChR2(H134R)_eYFP-WPRE-hGH (1×10^{12} GC, 500 nl, ~100–200 nl/min).

673

In vitro electrophysiological recordings

Slice preparation, solutions and recordings.

676 Brain slice preparation, storage and recordings were performed essentially as described

677 (Fernandez et al., 2018). Adult 8- 10-week-old C57BL6/J and VGAT-Ires-Cre mice (3 – 4 weeks

678 post viral injection) were briefly anesthetized with isoflurane and their brains quickly extracted.

679 Acute 300-µm-thick coronal brain slices were prepared in ice-cold oxygenated sucrose solution

680 (which contained in mM: 66 NaCl, 2.5 KCl, 1.25 NaH_2PO_4, 26 $NaHCO_3$, 105 D(+)-saccharose, 27

681 D(+)-glucose, 1.7 L(+)-ascorbic acid, 0.5 $CaCl_2$ and 7 $MgCl_2$), using a sliding vibratome (Histocom,

682 Zug, Switzerland). Slices were kept for 30 min in a recovery solution at 35°C (in mM: 131 NaCl,

683 2.5 KCl, 1.25 NaH_2PO_4, 26 $NaHCO_3$, 20 D(+)-glucose, 1.7 L(+)-ascorbic acid, 2 $CaCl_2$, 1.2 $MgCl_2$,

684 3 myo-inositol, 2 pyruvate) before being transferred to room temperature for at least 30 min before

685 starting the recording. Slices were placed in the recording chamber of an upright microscope

686 (Olympus BX50WI, Volketswil, Switzerland) and continuously perfused at room temperature with

687 oxygenated ACSF containing (in mM): 131 NaCl, 2.5 KCl, 1.25 NaH_2PO_4, 26 $NaHCO_3$, 20 D(+)-

688 glucose, 1.7 L(+)-ascorbic acid, 2 $CaCl_2$ and 1.2 $MgCl_2$. This solution was supplemented in all

689 experiments with 0.1 picrotoxin, 0.01 glycine, with picrotoxin removed for the recordings testing

690 for feedforward inhibition (see Fig. 4). Borders of anterior TRN and ATN+ were visually identified

691 in transillumination using a 10x water-immersion objective. Within a selected nucleus, cells were

692 visualized through differential interference contrast optics a 40x water-immersion objective.

693 Infrared images were acquired with an iXon Camera X2481 (Andor, Belfast, Northern Ireland).

694 Cells were patched using borosilicate glass pipettes (TW150F-4) (World Precision Instruments,

695 Sarasota, FL) pulled with a DMZ horizontal puller (Zeitz Instruments, Martinsried, Germany) to a

696 final resistance of 2.5-5 MΩ. A K^+-based intracellular solution that contained (in mM) 140

697 KGluconate, 10 Hepes, 10 KCl, 0.1 EGTA, 10 phosphocreatine, 4 Mg-ATP, 0.4 Na-GTP, pH 7.3,

698 290–305 mOsm, supplemented with ~2 mg/ml of neurobiotin (Vector Labs, Servion, Switzerland)

699 was used for comparative measurements of the passive cellular properties (Fig. 2B,2C), for the

700 cell-attached recordings (Fig. 3C) and for all current-clamp recordings (Fig. 3E). A Cs^+-based

701 intracellular solution containing (in mM) 127 CsGluconate, 10 Hepes, 2 CsBAPTA, 6 $MgCl_2$, 10

702 phosphocreatine, 2 Mg-ATP, 0.4 Na-GTP, 2 QX314-Cl, supplemented with ~2 mg/ml of

703 neurobiotin, pH 7.3, 290–305 mOsm) was used with all the other voltage-clamp protocols. For

704 these solutions, a liquid junction potential of -10 mV was taken into account for the current-clamp

705 data. Signals were amplified using a Multiclamp 700B amplifier, digitized via a Digidata1322A and

706 sampled at 10 kHz with Clampex10.2 (Molecular Devices, San José, CA).

Recording protocols, optogenetic stimulation and analysis.

708 Immediately after gaining whole-cell access, cell resistance (R_m) and cell capacitance (C_m) were

709 measured in voltage-clamp at -60 mV through applying 500 ms-long, 10-20 mV hyperpolarizing

710 steps (5 steps/cell). Then the recording was switched to current-clamp to measure the resting

711 membrane potential (RMP). Squared somatic current injections (-50 to -300 pA for 500 ms, 4

712 injections/cell) hyperpolarized neurons below -100 mV from membrane potentials between -50 to

713 -60 mV and induced repetitive burst discharge in TRN neurons and single burst discharge in

714 thalamic neurons (Fig. 2B, 2C). Squared current injections of increasing amplitude (step size, 50

715 pA, 500 ms) were used to depolarize the neurons and generate tonic firing. Action potential

716 properties were measured at the rheobase.

717 Whole-field blue LED (Cairn Res, Faversham, UK) stimulation (455 nm, duration: 0.1 to 1 ms,

718 maximal light intensity 3.5 mW, 0.16 mW/mm^2) in voltage-clamp (-60 mV) was used to assess the

719 connectivity of TRN and ATN+ neurons through fibers arising from the PreS/RSC. EPSCs were

720 elicited through single light pulses every 20 s, with a 5 mV hyperpolarizing step to control for the

721 access resistance. After a stable baseline of > 2 min, drugs were applied in the bath (40 µM

722 DNQX, 100 µM D,L-APV). To measure NMDA-components, the holding membrane potential was

723 slowly brought to +40 mV where NMDAR-mediated currents were recorded for 2 min before bath-

724 application of D,L-APV. Single light pulses were used in protocols to measure EPSC kinetics and

725 pharmacological properties (Fig. 2D, 2E). The latency from LED onset, EPSC half-width and

726 EPSC weighted decay time constant were measured with Clampfit 10.2. The effect of bath-

727 application of 40 µM DNQX was measured once the reduction of EPSC amplitude reached a

728 steady state. The NMDA/AMPA ratio was measured by dividing the amplitude of the EPSC at +40

729 mV in DNQX by the amplitude of the EPSC at -60 mV during the baseline and was expressed in

730 percentage.

731 Minimal stimulation was achieved by progressively reducing the intensity of a single light pulse

732 from its maximum (3.5 mW) to a level where only ~50 % of the stimuli induced a successful EPSC.

733 The light intensity potentiometer allowing a limited graduation of light intensities, we could include

734 only a few cells (n=12/50) in which this condition was achieved at 0.28±0.05 mW. In the case of

735 LD neurons, which showed very high amplitude EPSCs with frequent escape currents, none of

736 them reached the criterion to be included. Minimal stimulation was observed for light intensities

737 averaging 0.28±0.05 mW, less than 10 % of the maximum. In a subset of cells (n=8), we slightly

738 increased light intensity to 0.40±0.08 mW to verify whether failure rate decreased but the

739 amplitude of successful responses was maintained. This was achieved in 5 cells in which failure

740 rate decreased to 0 % but the amplitude of successes was 109±4 % of that found during minimal

741 stimulation, whereas it increased to > 140 % in the remaining 3 cases. All successful EPSCs at

742 minimal light stimulation were visually identified and measured in Clampfit10.2.

743 Cell-attached recordings of TRN cells (Fig. 3C) were achieved with recording pipettes of ~5 MΩ

744 resistance, voltage-clamped at 0 mV and ~0 pA of holding current, while applying single light

745 stimuli at varying light intensity (~100 stimuli/cell, one every 10 s). Whole-cell access was then

746 established and cells held in current-clamp at their resting membrane potential. Single light

747 stimulations with similar light intensities were given ~30 times for each cell every 10 s. The number

748 of action currents/action potentials and the interspike interval (ISI) were manually measured on

749 Clampfit10.2. The number of spikes was normalized to the maximum number evoked by the light

750 stimulation. Data were grouped in bins of 0.25 mW of light (Fig. 3C3) and a sigmoidal fit was

751 applied using Igor Pro 7 (WaveMetrics Inc., Lake Oswego, OR). The sigmoidal fit for cell-attached

752 evoked spikes was $= \frac{-78+160}{1+e^{\frac{-(x-0.18)}{0.32}}}$. The sigmoid fit for whole-cell evoked spikes was $= \frac{-142+232}{1+e^{\frac{-(x-0.2)}{0.73}}}$.

753 Paired light stimulations at 1, 2, 5, 10 and 20 Hz were used to assess the short-term plasticity of

754 PreS/RSC-TRN and PreS/RSC-ATN+ synapses. The paired pulse ration (PPR) was expressed

755 as the ratio between the second and the first EPSC amplitude (Fig. 3D). Four responses were

756 elicited for each frequency, with an interval of 20 s between each protocol. The amplitude of

757 EPSCs was measured on the average trace in Clampfit10.2, and traces were not included if

758 spontaneous currents appeared in between the paired stimuli.

759 For train stimulation, PreS-RSC afferents to TRN and ATN+ neurons were stimulated with 10 light

760 pulses delivered 1/30 s at 2, 5, 8 and 10 Hz while cells were held at -50 to -60 mV in current-

761   clamp (Fig. 3E). Per stimulation frequency and cell, 5 responses were recorded and averaged.

762   Responses were subdivided into sustained (Fig. 3E1) or entrained (Fig. 3E2) responses based

763   on whether or not the first light pulse elicited an action potential. The number of action potentials

764   generated by the train of stimulation was counted on Clampfit10.2. To quantify sustained and

765   entrained responses, the number of action potentials during the 5 first stimulations was compared

766   to the number of action potentials during the 5 last stimulations. In subthreshold responses, the

767   amplitudes of the phasic responses were calculated from the point of positive inflection after a

768   light stimulation to the next positive peak for each of the 10 subthreshold responses. The

769   persistent depolarization was measured as the difference between the baseline value before the

770   train of stimulation and the point of positive inflexion after each light stimulation. The mean

771   persistent depolarization for the last 3 stimulations was used to quantify the steady state

772   response.

773   To record feedforward inhibitory currents, using the Cs-based intracellular solution defined above,

774   we studied single light-evoked EPSCs recorded in ATN+ cells at -60 mV (uncorrected for a 10

775   mV junction potential). Then the membrane potential of the cell was slowly brought to +15 mV

776   (uncorrected for a 10 mV junction potential). In 6 ATN+ cells, IPSCs were recorded for 4 min (12

777   protocols, once every 20 s) for a baseline, then 10 µM gabazine were bath-applied. The amplitude

778   of the IPSCs in gabazine was measured at the steady state. A similar protocol was applied for 10

779   ATN+ cells recorded in VGAT-Ires-Cre mice expressing the inhibitory DREADD in TRN cells.

780   Instead of gabazine, 10 µM CNO were bath-applied after the baseline recording of IPSCs.

781   Measures of charge transfer were used to take into account the variable waveform of the IPSCs

782   that were composed of multiple superimposed burst-like synaptic events.

783   To determine the connectivity of PV- and Sst-expressing TRN cells, brain slices were prepared

784   from PV-Cre and Sst-Cre lines previously injected with ChR2-expressing virus (see above). Using

785   identical recording and light stimulation conditions, evoked IPSCs were quantified in neurons

786   recorded in the different thalamic nuclei AD, AV and LD.

In vivo single-unit recordings and head-direction monitoring

Electrode and fiber preparation.

789   Two types of recording configurations were used. Multi-wire electrodes were implanted for

790   studying response properties of ATN+ to PreS/RSC stimulation. Silicon probes were used for

791   identification and recording of HD-tuned units in combination with chemogenetic silencing of the

792   anterodorsal TRN.

793　The multi-wire electrodes consisted of 16 individually insulated nichrome wires (13-µm inner

794　diameter, impedance 1 – 3 MΩ; California Fine Wire) contained in a 26-gauge stainless steel

795　guide canula. The wires were attached to a 16-pin connector (CON/16m-V-t, Omnetics) (Courtin

796　et al., 2014), cut at a length of ~2 mm from the edge of the metal guiding tube and gold-plated

797　using a nanoZ™ device (White Matter LLC, provided by Plexon Inc., Dallas, TX) to a final

798　impedance of 50 – 100 kΩ. A silver wire (Warner Instr.) was soldered to the ground pin of the

799　connector. Two animals were implanted with a single shank linear silicone probe (Neuronexus

800　A1x16-5mm-50-703-Z16).

801　The optic fibers were built from a standard hard cladding multimode fiber (225 µm outer diameter,

802　Thorlabs, BFL37-2000/FT200EMT), inserted and glued (Heat-curable epoxy, Precision Fiber

803　Products, ET-353ND-16OZ) to a multimode ceramic zirconia ferrule (Precision Fiber Products,

804　MM-FER2007C-2300). The penetrating end was cut at the desired length (~2 mm) with a Carbide-

805　tip fiber optic scribe (Precision Fiber Products, M1-46124). The other end was polished with fiber-

806　polishing films (Thorlabs). The optic fibers were connected to a PlexBright Optogenetic

807　Stimulation System (Plexon) via home-made patch chord. The connection to the PlexBright Table-

808　top LED Module (Wavelength 465 nm) was achieved through a Mini MM FC 900µm Connector

809　(Precision Fiber Products, MM-CON2004-2300-14-BLK). The other end of the patch chord was

810　inserted into a ceramic zirconia ferrule, fixed with glue and heat-shrinking tube (Allied Electronics,

811　689-0267) and polished. Before the recording, the patch chord was attached to the implanted

812　optic fiber via a ceramic split sleeve (Precision Fiber Products, SM-CS125S).

813　## Surgery.

814　Virally injected C57BL6/J and VGAT-Ires-Cre mice were anesthetized with 5 % isoflurane, fixed

815　on a stereotaxic frame and kept on a feedback-controlled heating pad (Phymep). The level of

816　isoflurane was reduced along the surgery until 1 % and mixed with N_2O. Craniotomies were

817　opened above the PreS (AP, ML, DV: -3.8, +/-2.5, -1.7), the left ATN (AP, ML, DV: -0.8, +0.75, -

818　2.8) and the lateral cerebellum with a microdrill (1/005 drill-size). The conjunctive tissue on the

819　skull was removed with a scalpel and the skull was cleaned with iodine-based disinfectant. The

820　skull was then scratched with the tip of the scalpel in a grid-like meshwork of grooves to improve

821　the attachment of the glue (Loctite 401, Koening). Multi-wire electrodes and linear silicone probes

822　were lowered vertically, at approximately 10 µm/s initially and then 1 µm/s when reaching the ATN

823　and glued to the skull. Optic fibers were lowered vertically above the PreS at similar rates. For

824　the multi-wire electrodes, the ground silver wire was implanted at the surface of the lateral

825　cerebellum. For silicone probes, the reference and ground wires were twisted together and

826   implanted at the surface of the lateral cerebellum. Carprofen (5 mg/kg, i.p.) and paracetamol (2

827   mg/mL, drinking water) were provided during the peri-operative period. The mice were left in their

828   home cage for a week to recover from the surgery and their weight, behavior and all aspects were

829   monitored in score sheets established with the veterinary protocols. During this period, mice were

830   also habituated to the handling and the recording cables.

831   <u>Unit recordings and HD monitoring</u>.

832   Mice were placed into a large cylindrical Plexiglas cage (diameter: 50 cm, height: 40 cm) where

833   they could freely behave all along the recording sessions. The cage was positioned below a vision

834   color camera inside a Faraday cage. Implanted animals were connected to the pre-amplifier PZ5-

835   32 (Tucker-Davis Technologies (TDT)) via a ZIF-Clip Headstage adaptor (TDT, ZCA-OMN16) for

836   the multi-wire electrodes and a ZIF-Clip Headstage (TDT) for the silicone probes. The camera

837   was connected to a RV2 collection device (TDT) capable of tracking red and green LEDs mounted

838   on the ZIF-Clip Headstage. The preamplifier was connected to a main amplifier RZ5D (TDT). The

839   main computer (WS8, TDT) used the Real-time Processor Visual Design Studio (RPvdsEx) tool

840   to design the recording sessions, activate light stimulation from the PlexBright Optogenetic

841   Stimulation System (Plexon), and acquire the electrophysiological data from the headstage and

842   tracking data from the camera.

843   For C57Bl6/J mice implanted with a multi-wire electrode, a recording session consisted in a 10 –

844   20 min baseline recording followed by a 10 – 20 min recording with optogenetic activation of the

845   PreS/RSC. The stimulation consisted in 300 – 600 light stimulations of 10 ms duration, one

846   stimulation every 2 s. The intensity of the light ranged from 2 – 6 mW depending on the quality of

847   the homemade optic fibers. For VGAT-Ires-Cre mice implanted with a silicone probe, a recording

848   session consisted in a 10 – 20 min baseline recording, i.p. injection of CNO (1 – 2 mg/kg) or NaCl,

849   40 min resting in homecage and 10 – 20 min test recording. The timing of the CNO injection is

850   based on previous *in vivo* work using the same mouse line and CNO products, showing that the

851   CNO effect peaked ~30 min post i.p. injection (Fernandez et al., 2018).

852   <u>Spike sorting.</u>

853   The Offline Sorter software (Plexon), Neuroexplorer (Nex Technologies) and MATLAB

854   (MathWorks) were used to sort and analyze single-unit spikes. The waveforms were manually

855   delineated in the two-dimensional space of principal components using their voltage features.

856   Single units were defined as discrete clusters of waveforms in the principal component space,

857   and did not contain spikes with a refractory period less than 1 ms. The quantification of the clusters

858 separation was further measured with multivariate ANOVA and J3 statistics. Cross-correlation

859 analyses were used to control that a single unit was not recorded on multiple channels. Target

860 units that had a peak of spike discharge when the reference unit fired were considered as

861 duplicates and only one of the copy was used for analysis (Adapted from (Rozeske et al., 2018)).

862 To compare the recordings during baseline and after injection of CNO, units were sorted with two

863 different methods. At first, both recording sessions were manually sorted as described above

864 while the experimenter was blind to the baseline/CNO condition. In a second step, the baseline

865 sorting template was used for the CNO recording. Both methods gave similar results and only the

866 manual sorted data are shown.

867 <u>Unit analysis.</u>

868 The discharge pattern of well-defined single units in the ATN+ was aligned to the optogenetic

869 stimulation using peri-event raster plots and cumulative histogram (5 ms bins, starting 50 ms

870 before LED onset and lasting 200 ms after LED onset, Neuroexplorer). The firing rate 50 ms

871 before the LED onset was used as a baseline to calculate the Z-score of each bin as follow: =

872 $\frac{measured\ valued - baseline\ average}{baseline\ standard\ error}$. Z-scores were considered significant when > 1.96 and < -1.96.

873 Significant changes in the firing rate fell into 4 distinct classes depending on the direction of the

874 change (increase or decrease firing) and the timing of the change.

875 Using a custom-made Matlab routine, the discharge patterns of ATN+ units were binned to the

876 HD of the mice. The angles of direction were binned in 6°. The firing rate was averaged for each

877 of the 60 portions of the circle. The length of the Rayleigh vector (r) was calculated and units were

878 considered as HD if r ≥ 0.4, as head-modulated if 0.2 ≤ r < 0.4 and as not tuned if r < 0.2 (Yoder

879 and Taube, 2009). The maximal firing rate, the width and the preferred direction were calculated

880 for HD units. The width of the tuning curve was measured as the span of the angle between the

881 two directions for which the firing rate was equal to 50 % of the maximal firing rate at the preferred

882 direction (Blair and Sharp, 1995).

883

884 **Behavioral experiment**

885 Recording.

886 One week before the beginning of the behavioral task, VGAT-Ires-Cre mice expressing either an
887 inhibitory DREADD (DREADD mice) or a non DREADD-related (control mice) construct into the
888 anterodorsal TRN were habituated to the handling and i.p. injection. Naïve VGAT-Ires-Cre male
889 mice were trained to find a 12 cm wide circular platform submerged 0.5 – 0.8 cm below the surface
890 in a 150 cm diameter circular pool filled with white opaque water at 23±1°C. Mice were trained in
891 daily sessions composed of 4 consecutive trials, with a 60 s probe session without the platform
892 preceding the first trial session every odd days. A trial ended when the mice spent 5 s onto the
893 platform. Mice were left 10 s more before being placed below a heating lamp before the next trial,
894 10 – 15 s later. Four shapes around the pool (cross, horizontal stripes, vertical stripes, coffee
895 grain) served as visual cues and were placed in the SW, NW, NE, SE corner of the room
896 respectively. If the mouse failed to find the platform after 60 s, the experimenter guided it to the
897 platform where it was left for 15 s. Mice were placed in the pool facing the wall. The position of
898 pool entry was randomly shuffled every day between NE, SE, NW and NE. During a 60 s probe
899 session, the platform was removed and mice were released from the wall of the quadrant opposite
900 to the target one. The experimenter was blind to the condition of the mice (control or DREADD).
901 The session duration (between the first and the last animal) was ~2 hours, the first trial starting at
902 Zeitgeber time 0 + 1.5 h. Daily i.p. injection of CNO (1 – 2 mg/kg) were performed 40 min before
903 the beginning of the session. The timing of the CNO injection is based on previous *in vivo* work
904 using the same mouse line and CNO products, showing that the CNO effect peaked ~30 min post
905 i.p. injection (Fernandez et al., 2018).

906 Analysis and automatic strategy detection.

907 The video tracking data were analyzed using EthoVisionXT14 (Noldus) to quantify the average
908 swimming speed, escape latency, proximity (mean distance of all the tracked points of the path
909 to the platform center), percentage time spent in target quadrant and platform crossings.
910 Heatmaps were generated by superimposing all the path points of every mouse in a group.
911 Heatmaps were linearly scaled using the global minimum and maximum for both groups to allow
912 comparison between the two. To attribute a specific strategy to each MWM trial, we used a
913 homemade matlab algorithm based on (Garthe et al., 2009). For each trial, the animal path in the
914 MWM was extracted as timed-tagged x and y coordinates from which specific variables were
915 computed in order to take a decision. The 8 strategies are described in Suppl. Fig. 5 and the

916 decision was made in the following sequential order with the 4 allocentric strategies first followed
917 by the 4 egocentric strategies: 1-Direct swimming; if 95 % of the time-points are spent in the goal
918 cone (isosceles triangle with its height going from starting point to goal platform with an origin
919 angle of 40°). 2-Focal search; if the mean distance of the path to its centroid (MDTC) was inferior
920 to 35 % standard unit (STDU) corresponding to the radius of the MWM, and the mean distance
921 to the edge of the goal platform was inferior to 30% STDU. 3-directed search; if total time spent
922 in the goal cone was superior to 80 %. 4-perseverance; if the MDTC was inferior to 45 % STDU
923 and the mean distance to the previous platform edge was inferior to 40 % STDU. In our case, the
924 perseverance strategy was only possible after day 10, during the reversal learning period. 5-
925 chaining; if the time spent in the annulus zone (spanning from 33 to 70 % STDU) was superior to
926 80 %. 6-scanning; if the total coverage of the MWM (the pool was divided in 15 cm squares and
927 the coverage was obtained as the ratio of crossed squares over the total number of squares) was
928 superior to 10% and inferior to 60 %, and the mean distance of the path to the center of the MWM
929 was inferior to 70% STDU. 7-thigmotaxis; if the time spent in the closer wall zone (spanning from
930 87 % STDU to the edge of the MWM) was superior to 35 % and the time spend in the wider wall
931 zone (spanning from 70 % STDU to the edge of the MWM) was superior to 65 %. 8-random
932 search; if the total coverage of the MWM was superior to 60 %. If none the conditions could be
933 met in this order, no strategy were attributed.

Statistics

935 All tests were done using R programming software (2.15.0, R Core Team, The R Foundation for
936 Statistical Computing (www.rproject.org/foundation), 2007]. The normality of the data sets was
937 assessed using Shapiro-Wilk normality test. Comparison of two data sets were done using
938 Student's *t* test and paired Student's *t* test, for non-repeated and repeated measures respectively,
939 or their non-parametric equivalent, Mann-Whitney U test and Wilcoxon signed rank-test. Chi-
940 square tests were used to assess whether the swimming region of mice during probe sessions of
941 the MWM were different from the expected frequencies and the proportion of strategies used
942 between mouse groups. 1-way/2-way (non-)repeated measure ANOVAs followed by post hoc *t*
943 tests were used when necessary on normally distributed data sets whereas non-normally
944 distributed data were analyzed directly with the post hoc tests. A Bonferroni correction was
945 applied when more than two comparisons were done on the same data set and the new alpha
946 threshold is indicated. All statistical tests are specifically indicated in the figure legends if they are
947 not given in the main text.

948

References

949

950 Ahrens S, Jaramillo S, Yu K, Ghosh S, Hwang GR, Paik R, Lai C, He M, Huang ZJ, Li B (2015) ErbB4 regulation
951   of a thalamic reticular nucleus circuit for sensory selection. Nat Neurosci 18:104-111.

952 Astori S, Lüthi A (2013) Synaptic plasticity at intrathalamic connections via Ca$_V$3.3 T-type Ca^{2+} channels and
953   GluN2B-containing NMDA receptors. J Neurosci 33:624-630.

954 Awasthi A, Ramachandran B, Ahmed S, Benito E, Shinoda Y, Nitzan N, Heukamp A, Rannio S, Martens H,
955   Barth J, Burk K, Wang YT, Fischer A, Dean C (2019) Synaptotagmin-3 drives AMPA receptor
956   endocytosis, depression of synapse strength, and forgetting. Science 363.

957 Blair HT, Sharp PE (1995) Anticipatory head direction signals in anterior thalamus: evidence for a
958   thalamocortical circuit that integrates angular head motion to compute head direction. J Neurosci
959   15:6260-6270.

960 Bubb EJ, Kinnavane L, Aggleton JP (2017) Hippocampal - diencephalic - cingulate networks for memory
961   and emotion: An anatomical guide. Brain Neurosci Adv 1.

962 Butler WN, Smith KS, van der Meer MAA, Taube JS (2017) The head-direction signal plays a functional role
963   as a neural compass during navigation. Curr Biol 27:2406.

964 Calton JL, Taube JS (2005) Degradation of head direction cell activity during inverted locomotion. J
965   Neurosci 25:2420-2428.

966 Castro-Alamancos MA, Calcagnotto ME (1999) Presynaptic long-term potentiation in corticothalamic
967   synapses. J Neurosci 19:9090-9097.

968 Clark BJ, Bassett JP, Wang SS, Taube JS (2010) Impaired head direction cell representation in the
969   anterodorsal thalamus after lesions of the retrosplenial cortex. J Neurosci 30:5289-5302.

970 Clark BJ, Simmons CM, Berkowitz LE, Wilber AA (2018) The retrosplenial-parietal network and reference
971   frame coordination for spatial navigation. Behav Neurosci 132:416-429.

972 Clemente-Perez A, Makinson SR, Higashikubo B, Brovarney S, Cho FS, Urry A, Holden SS, Wimer M, David
973   C, Fenno LE, Acsády L, Deisseroth K, Paz JT (2017) Distinct thalamic reticular cell types differentially
974   modulate normal and pathological cortical rhythms. Cell Rep 19:2130-2142.

975 Cornwall J, Cooper JD, Phillipson OT (1990) Projections to the rostral reticular thalamic nucleus in the rat.
976   Exp Brain Res 80:157-171.

977 Courtin J, Chaudun F, Rozeske RR, Karalis N, Gonzalez-Campo C, Wurtz H, Abdi A, Baufreton J, Bienvenu
978   TC, Herry C (2014) Prefrontal parvalbumin interneurons shape neuronal activity to drive fear
979   expression. Nature 505:92-96.

980 Crabtree JW (2018) Functional diversity of thalamic reticular subnetworks. Front Syst Neurosci 12:41.

981 Crandall SR, Cruikshank SJ, Connors BW (2015) A corticothalamic switch: controlling the thalamus with
982   dynamic synapses. Neuron 86:768-782.

983 Cruikshank SJ, Urabe H, Nurmikko AV, Connors BW (2010) Pathway-specific feedforward circuits between
984   thalamus and neocortex revealed by selective optical stimulation of axons. Neuron 65:230-245.

985 Ding SL (2013) Comparative anatomy of the prosubiculum, subiculum, presubiculum, postsubiculum, and
986   parasubiculum in human, monkey, and rodent. J Comp Neurol 521:4145-4162.

987 Dolleman-van der Weel MJ, Morris RG, Witter MP (2009) Neurotoxic lesions of the thalamic reuniens or
988   mediodorsal nucleus in rats affect non-mnemonic aspects of watermaze learning. Brain Struct
989   Funct 213:329-342.

990 Dong P, Wang H, Shen XF, Jiang P, Zhu XT, Li Y, Gao JH, Lin S, Huang Y, He XB, Xu FQ, Duan S, Lian H, Wang
991   H, Chen J, Li XM (2019) A novel cortico-intrathalamic circuit for flight behavior. Nat Neurosci
992   22:941-949.

993 Dumont JR, Taube JS (2015) The neural correlates of navigation beyond the hippocampus. Prog Brain Res
994   219:83-102.

995   Fernandez LM, Vantomme G, Osorio-Forero A, Cardis R, Béard E, Lüthi A (2018) Thalamic reticular control
996   of local sleep in mouse sensory cortex. Elife 7.
997   Fernandez LMJ, Pellegrini C, Vantomme G, Béard E, Lüthi A, Astori S (2017) Cortical afferents onto the
998   nucleus Reticularis thalami promote plasticity of low-threshold excitability through GluN2C-
999   NMDARs. Sci Rep 7:12271.
1000   Garthe A, Kempermann G (2013) An old test for new neurons: refining the Morris water maze to study
1001   the functional relevance of adult hippocampal neurogenesis. Front Neurosci 7:63.
1002   Gentet LJ, Ulrich D (2004) Electrophysiological characterization of synaptic connections between layer VI
1003   cortical cells and neurons of the nucleus reticularis thalami in juvenile rats. Eur J Neurosci 19:625-
1004   633.
1005   Gjoni E, Zenke F, Bouhours B, Schneggenburger R (2018) Specific synaptic input strengths determine the
1006   computational properties of excitation-inhibition integration in a sound localization circuit. J
1007   Physiol 596:4945-4967.
1008   Golshani P, Liu XB, Jones EG (2001) Differences in quantal amplitude reflect GluR4- subunit number at
1009   corticothalamic synapses on two populations of thalamic neurons. Proc Natl Acad Sci U S A
1010   98:4172-4177.
1011   Gonzalo-Ruiz A, Lieberman AR (1995a) Topographic organization of projections from the thalamic reticular
1012   nucleus to the anterior thalamic nuclei in the rat. Brain Res Bull 37:17-35.
1013   Gonzalo-Ruiz A, Lieberman AR (1995b) GABAergic projections from the thalamic reticular nucleus to the
1014   anteroventral and anterodorsal thalamic nuclei of the rat. J Chem Neuroanat 9:165-174.
1015   Goodridge JP, Taube JS (1997) Interaction between the postsubiculum and anterior thalamus in the
1016   generation of head direction cell activity. J Neurosci 17:9315-9330.
1017   Halassa MM, Chen Z, Wimmer RD, Brunetti PM, Zhao S, Zikopoulos B, Wang F, Brown EN, Wilson MA
1018   (2014) State-dependent architecture of thalamic reticular subnetworks. Cell 158:808-821.
1019   Herrera CG, Cadavieco MC, Jego S, Ponomarenko A, Korotkova T, Adamantidis A (2016) Hypothalamic
1020   feed-forward inhibition of thalamocortical network controls arousal and consciousness. Nat
1021   Neurosci 19:290-298.
1022   Huguenard JR (1996) Low-threshold calcium currents in central nervous system neurons. Annu Rev Physiol
1023   58:329-348.
1024   Krol A, Wimmer RD, Halassa MM, Feng G (2018) Thalamic reticular dysfunction as a circuit endophenotype
1025   in neurodevelopmental disorders. Neuron 98:282-295.
1026   Krout KE, Loewy AD, Westby GW, Redgrave P (2001) Superior colliculus projections to midline and
1027   intralaminar thalamic nuclei of the rat. J Comp Neurol 431:198-216.
1028   Le Masson G, Renaud-Le Masson S, Debay D, Bal T (2002) Feedback inhibition controls spike transfer in
1029   hybrid thalamic circuits. Nature 417:854-858.
1030   Lee SM, Friedberg MH, Ebner FF (1994) The role of GABA-mediated inhibition in the rat ventral posterior
1031   medial thalamus. II. Differential effects of GABAA and GABAB receptor antagonists on responses
1032   of VPM neurons. J Neurophysiol 71:1716-1726.
1033   Lozsádi DA (1994) Organization of cortical afferents to the rostral, limbic sector of the rat thalamic
1034   reticular nucleus. J Comp Neurol 341:520-533.
1035   Lozsádi DA (1995) Organization of connections between the thalamic reticular and the anterior thalamic
1036   nuclei in the rat. J Comp Neurol 358:233-246.
1037   Miniaci MC, De Leonibus E (2018) Missing the egocentric spatial reference: a blank on the map. F1000Res
1038   7:168.
1039   Mitchell AS, Czajkowski R, Zhang N, Jeffery K, Nelson AJD (2018) Retrosplenial cortex and its role in spatial
1040   cognition. Brain Neurosci Adv 2:2398212818757098.
1041   Paré D, Steriade M, Deschênes M, Oakson G (1987) Physiological characteristics of anterior thalamic
1042   nuclei, a group devoid of inputs from reticular thalamic nucleus. J Neurophysiol 57:1669-1685.

1043 Perry BAL, Mitchell AS (2019) Considering the evidence for anterior and laterodorsal thalamic nuclei as
1044   higher order relays to cortex. Front Mol Neurosci 12:167.
1045 Peyrache A, Schieferstein N, Buzsáki G (2017) Transformation of the head-direction signal into a spatial
1046   code. Nat Commun 8:1752.
1047 Peyrache A, Lacroix MM, Petersen PC, Buzsáki G (2015) Internally organized mechanisms of the head
1048   direction sense. Nat Neurosci 18:569-575.
1049 Peyrache A, Duszkiewicz AJ, Viejo G, Angeles-Duran S (2019) Thalamocortical processing of the head-
1050   direction sense. Prog Neurobiol:101693.
1051 Pinault D (2004) The thalamic reticular nucleus: structure, function and concept. Brain Res Brain Res Rev
1052   46:1-31.
1053 Pinault D, Deschênes M (1998) Projection and innervation patterns of individual thalamic reticular axons
1054   in the thalamus of the adult rat: a three-dimensional, graphic, and morphometric analysis. J Comp
1055   Neurol 391:180-203.
1056 Rogers J, Churilov L, Hannan AJ, Renoir T (2017) Search strategy selection in the Morris water maze
1057   indicates allocentric map formation during learning that underpins spatial memory formation.
1058   Neurobiol Learn Mem 139:37-49.
1059 Rozeske RR, Jercog D, Karalis N, Chaudun F, Khoder S, Girard D, Winke N, Herry C (2018) Prefrontal-
1060   periaqueductal gray-projecting neurons mediate context fear discrimination. Neuron 97:898-910
1061   e896.
1062 Scheibel ME, Scheibel AB (1966) The organization of the nucleus reticularis thalami: a Golgi study. Brain
1063   Res 1:43-62.
1064 Sherman SM (2001) Thalamic relay functions. Prog Brain Res 134:51-69.
1065 Sherman SM (2017) Functioning of circuits connecting thalamus and cortex. Compr Physiol 7:713-739.
1066 Sherman SM, Guillery RW (1998) On the actions that one nerve cell can have on another: distinguishing
1067   "drivers" from "modulators". Proc Natl Acad Sci U S A 95:7121-7126.
1068 Sheroziya M, Timofeev I (2014) Global intracellular slow-wave dynamics of the thalamocortical system. J
1069   Neurosci 34:8875-8893.
1070 Simonnet J, Fricker D (2018) Cellular components and circuitry of the presubiculum and its functional role
1071   in the head direction system. Cell Tissue Res 373:541-556.
1072 Soto-Sánchez C, Wang X, Vaingankar V, Sommer FT, Hirsch JA (2017) Spatial scale of receptive fields in the
1073   visual sector of the cat thalamic reticular nucleus. Nat Commun 8:800.
1074 Stackman RW, Jr., Lora JC, Williams SB (2012) Directional responding of C57BL/6J mice in the Morris water
1075   maze is influenced by visual and vestibular cues and is dependent on the anterior thalamic nuclei.
1076   J Neurosci 32:10211-10225.
1077 Taube JS (1995) Head direction cells recorded in the anterior thalamic nuclei of freely moving rats. J
1078   Neurosci 15:70-86.
1079 Taube JS, Muller RU, Ranck JB, Jr. (1990) Head-direction cells recorded from the postsubiculum in freely
1080   moving rats. I. Description and quantitative analysis. J Neurosci 10:420-435.
1081 Taube JS, Kesslak JP, Cotman CW (1992) Lesions of the rat postsubiculum impair performance on spatial
1082   tasks. Behav Neural Biol 57:131-143.
1083 Tsanov M, Chah E, Vann SD, Reilly RB, Erichsen JT, Aggleton JP, O'Mara SM (2011) Theta-modulated head
1084   direction cells in the rat anterior thalamus. J Neurosci 31:9489-9502.
1085 Usrey WM, Sherman SM (2019) Corticofugal circuits: Communication lines from the cortex to the rest of
1086   the brain. J Comp Neurol 527:640-650.
1087 Valerio S, Taube JS (2012) Path integration: how the head direction signal maintains and corrects spatial
1088   orientation. Nat Neurosci 15:1445-1453.
1089 van der Meer MAA, Richmond Z, Braga RM, Wood ER, Dudchenko PA (2010) Evidence for the use of an
1090   internal sense of direction in homing. Behav Neurosci 124:164-169.

1091 van Groen T, Wyss JM (1990) The postsubicular cortex in the rat: characterization of the fourth region of
1092   the subicular cortex and its connections. Brain Res 529:165-177.
1093 Vantomme G, Osorio-Forero A, Lüthi A, Fernandez LMJ (2019) Regulation of local sleep by the thalamic
1094   reticular nucleus. Front Neurosci 13:576.
1095 Vong L, Ye C, Yang Z, Choi B, Chua S, Jr., Lowell BB (2011) Leptin action on GABAergic neurons prevents
1096   obesity and reduces inhibitory tone to POMC neurons. Neuron 71:142-154.
1097 Weese GD, Phillips JM, Brown VJ (1999) Attentional orienting is impaired by unilateral lesions of the
1098   thalamic reticular nucleus in the rat. J Neurosci 19:10135-10139.
1099 Wilkins LK, Girard TA, Herdman KA, Christensen BK, King J, Kiang M, Bohbot VD (2017) Hippocampal
1100   activation and memory performance in schizophrenia depend on strategy use in a virtual maze.
1101   Psychiatry Res Neuroimaging 268:1-8.
1102 Wimmer RD, Schmitt LI, Davidson TJ, Nakajima M, Deisseroth K, Halassa MM (2015) Thalamic control of
1103   sensory selection in divided attention. Nature 526:705-709.
1104 Wright NF, Erichsen JT, Vann SD, O'Mara SM, Aggleton JP (2010) Parallel but separate inputs from limbic
1105   cortices to the mammillary bodies and anterior thalamic nuclei in the rat. J Comp Neurol
1106   518:2334-2354.
1107 Yoder RM, Taube JS (2009) Head direction cell activity in mice: robust directional signal depends on intact
1108   otolith organs. J Neurosci 29:1061-1076.
1109 Yoder RM, Valerio S, Crego ACG, Clark BJ, Taube JS (2019) Bilateral postsubiculum lesions impair visual
1110   and nonvisual homing performance in rats. Behav Neurosci 133:496-507.
1111 Zikopoulos B, Barbas H (2007) Circuits formultisensory integration and attentional modulation through
1112   the prefrontal cortex and the thalamic reticular nucleus in primates. Rev Neurosci 18:417-438.
1113 Zikopoulos B, Barbas H (2012) Pathways for emotions and attention converge on the thalamic reticular
1114   nucleus in primates. J Neurosci 32:5338-5350.

1115